Chemical Engineering Journal 405 (2021) 126648

Contents lists available at ScienceDirect

Chemical Engineering Journal

journal homepage: www.elsevier.com/locate/cej

Fabrication strategies and Cr(VI) elimination activities of the MOF-derivatives and their composites

Yu-Xuan Li[a], Yong-Chun Han[a], Chong-Chen Wang[a,b,*]

[a] Beijing Key Laboratory of Functional Materials for Building Structure and Environment Remediation, School of Environment and Energy Engineering, Beijing University of Civil Engineering and Architecture, Beijing 100044, China
[b] College of Environmental Science and Engineering, North China Electric Power University, Beijing 102206, China

HIGHLIGHTS

- The fabrication strategies of MOF-derivatives and their composites were presented.
- The Cr(VI) removal behaviors of MOF-derivatives and their composites were reviewed.
- The possible mechanisms of Cr(VI) removal via different methods were highlighted.
- The involved challenges and prospects of Cr(VI) removal were proposed.

GRAPHICAL ABSTRACT

ARTICLE INFO

Keywords:
Metal–organic frameworks
Derivatives
Hexavalent chromium
Catalysis
Adsorption

ABSTRACT

Hexavalent chromium (Cr(VI)), as one of the hazardous heavy metals, has attracted increasing attention due to its toxicity, carcinogenicity along with the threat to the health and safety of aquatic organisms. The Cr(VI) removal methods mainly include adsorption and catalytic reduction. Metal-organic frameworks (MOFs) exhibit some merits like large surface area, inherent porous structure and adjustable topology. MOF-derivatives like porous carbon, metal oxides and metal sulfides can retain the merits of their MOFs precursors, which have been used in adsorption, catalysis, as well as energy storage and conversion. This review presented the state-of-the-art status of the MOF-derivatives and their composites for the purpose of Cr(VI) removal, in which the Cr(VI) removal mechanisms over the various MOF-derivatives and their composites were carefully introduced. Finally, the challenges and prospects of MOF derivatives and their composites in Cr(VI) removal from water were proposed.

1. Introduction

Heavy metals contained in industrial wastewater are one of the sources of water pollution [1]. The exposure of long-standing, hardly biodegradable and bioconcentrating heavy metals to the environment will exert negative effects on the ecosystem and human health [2]. As a typical heavy metal in wastewater, chromium was discharged mainly from the electroplating, photographic material, leather and other industries [3]. Chromium generally presents in the oxidation states of Cr (III) and Cr(VI) [4,5], in which Cr(VI), in the main forms of $HCrO_4^-$ or CrO_4^{2-} (Fig. 1a and 1b) [6], is more hazardous due to its high water solubility and strong carcinogenic effect on most organisms. It is worth

* Corresponding author at: Beijing Key Laboratory of Functional Materials for Building Structure and Environment Remediation, School of Environment and Energy Engineering, Beijing University of Civil Engineering and Architecture, Beijing 100044, China.
E-mail address: wangchongchen@bucea.edu.cn (C.-C. Wang).

https://doi.org/10.1016/j.cej.2020.126648
Received 22 June 2020; Received in revised form 9 August 2020; Accepted 10 August 2020
Available online 13 August 2020
1385-8947/

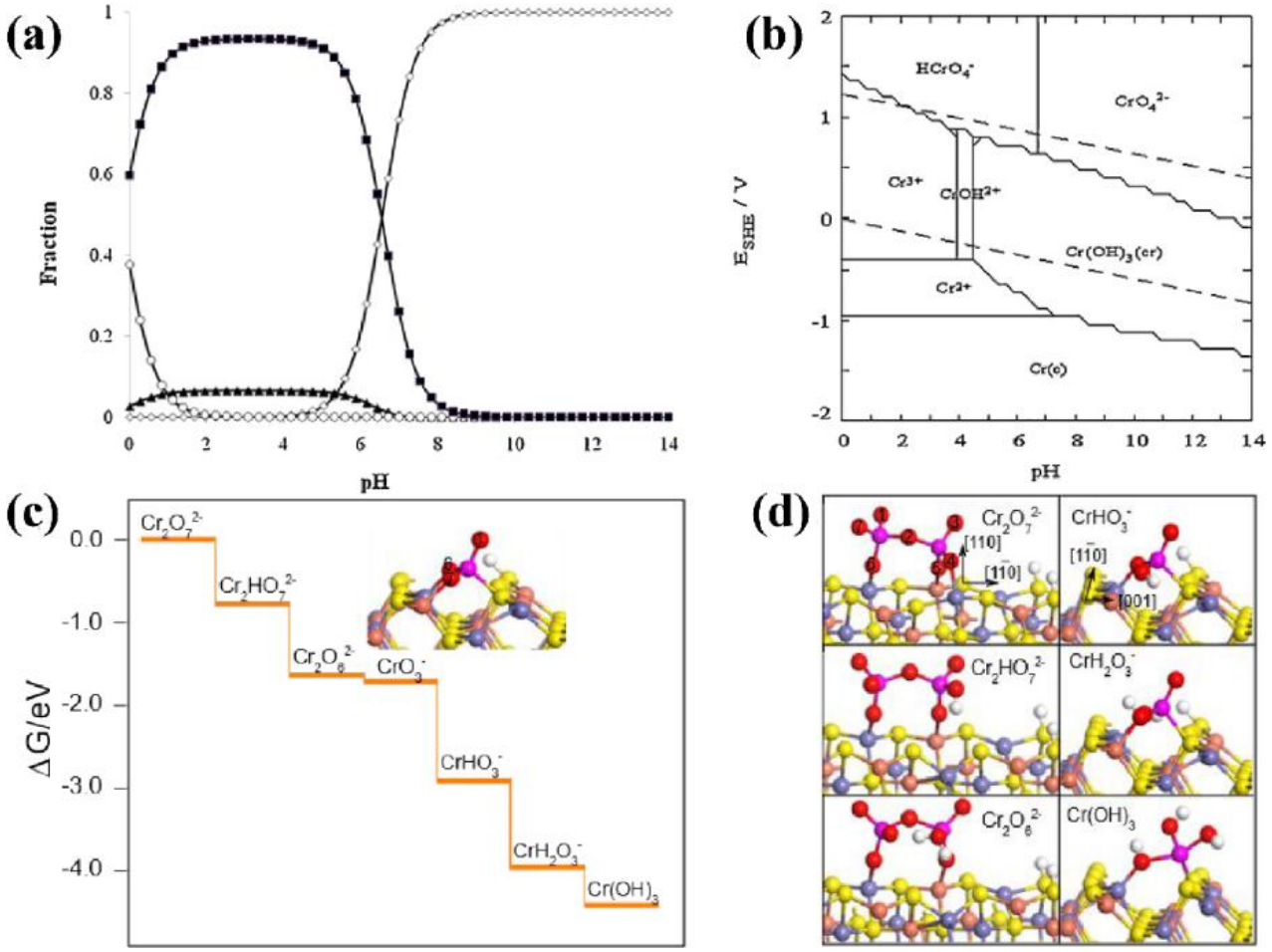

Fig. 1. (a) Dominant region of Cr(VI) chemicals in aqueous solution. (b) Pourbaix diagram for different chemical forms of Cr. [CrO_4^{2-}] = 2.00 mM, I = 0.005 M and T = 25 ℃. [6]. (◊) CrO_4^{2-}, (▲) $Cr_2O_7^{2-}$, (○) H_2CrO_4 and (■) $HCrO_4^-$. (c) The free energy surface and (d) optimized intermediates structures by DFT modelling of the Cr(VI) reduction dynamics. [21]. (Yellow, red, white, purple, blue, and orange spheres represent S, O, H, Cr, Fe, and Cu atoms, respectively.) (For interpretation of the references to colour in this figure legend, the reader is referred to the web version of this article.)

noting that Cr(VI) can easily penetrate into the body through digestion, the respiratory tract, skin and mucous membranes [7,8]. The Cr(VI) concentrations generally ranged from 0.5 mg L^{-1} in surface water to 270.0 mg L^{-1} in wastewater [9,10]. The World Health Organization (WHO) recommends that the limited concentration of total chromium is 50 μg L^{-1} in drinking water guidelines [11,12]. It was urgent to eliminate Cr(VI), even total Cr from water to guarantee the sustainable development and ecological environment. Up to now, the methods of Cr (VI) removal mainly include adsorption [13,14], reduction [15,16], chemical precipitation [17,18] and membrane filtration [19,20]. Among them, the most preferred and widely investigated methods for effectively treating Cr(VI)-containing wastewater are adsorption or reducing Cr(VI) to Cr(III). It was deemed that Cr(III) displayed lower toxicity and could be easily removed as $Cr(OH)_3$ precipitates under alkaline even neutral conditions, which was also confirmed the feasibility by density functional theory (DFT) modeling (Fig. 1c and 1d) [21]. Generally, the low-cost and easily available activated carbon and chitosan are used to accomplish adsorptive removal of Cr(VI) [22–24]. However, they suffered from limited adsorption capacities and adsorption efficiencies. As the common catalysts, precious metals (like Pd, Au) and ferrous metals (like Fe^0) are often introduced for catalytic Cr (VI) reduction with the aid of formic acid [25–27], while the leakage of precious metals or ferrous ions may result in the potential risk of secondary pollution. In addition, photocatalytic Cr(VI) reduction achieved over semiconductor photocatalysts (like TiO_2 and MoS_2) [28,29] usually suffered from smaller specific surface area and lower photocatalytic reduction efficiency.

Metal-organic frameworks (MOFs) are porous crystalline materials assembled from metal ions/clusters and organic linkers [30], which has arose wide interests in catalysis [31,32], adsorption [33–35], gas separation [36–38] and so on [39–44] due to their characteristics like large surface area, thermal stability, polymetallic sites and inherent porous structure [45,46]. Over the years, besides the earliest and most popular solvothermal method, some green and economical synthesis methods have been developed to promote the development and application of MOFs. Researchers continually explore efficient, economical, and high-throughput synthesis techniques to shorten the reaction time, avoid or reduce the use of organic solvents and achieve quantitative yield [47–49], including mechanochemical synthesis [50], microwave-assisted synthesis [51], sonochemical synthesis [52] and electrochemical synthesis [53].

Although MOFs have exhibited some outstanding performances, there are still some disadvantages to be overcome. For example, most MOFs possess micropores instead of mesopores, which is not conducive to the access of target pollutants. In addition, many MOFs are unstable in water, in which the destroy of bonding between metal ions and organic linkers may result in secondary pollution. In order to further improve the properties of MOFs, the preparation of derivatives with MOFs as precursors have received increasing attentions [54–56]. Firstly, the large-scale production strategies provide enough low-cost and plentiful MOFs for the preparation of derivatives. Secondly, the unique morphologies of MOFs can be further maintained well in the

obtained MOF-derivatives under appropriate treatment conditions [57]. MOF-derived materials possess various advantages originated from their templates, such as high porosity, ultra-high surface area and adjustable pore size. As well, MOF-derived materials can overcome the instability of MOFs to accomplish long cycle life [58]. MOF-derived materials have demonstrated good performances in the fields of catalysis [59–61], gas storage/separation [62,63], adsorption [64–66], along with energy storage and conversion [67–69]. Different MOF-derivatives like porous carbon materials, metal oxides, metal sulfides, and their composites can be obtained via different fabrication strategies.

Some cases illustrated that MOF-derivatives and their composites could be adopted for water treatment, including adsorptive or catalytic removal of contaminants like organic pollutants and heavy metal ions from water [70]. For example, N-doped carbon with MOF-5 as a template was used to achieve high-performance adsorption toward methylene blue (MB) [71]. Dong and coworkers utilized Pd@NPC (NPC derived from Ni-BTC) to remove chlorophenols via catalytic hydrochlorination [72]. Luo and coworkers prepared ZnO/$ZnFe_2O_4$/C with Fe^{III}-modified MOF-5 as a precursor to accomplish efficient uptake toward Pb(II) [73]. At present, the researches concerning the Cr(VI) removal with MOF-derivatives and their composites are tapping a new door, which will arise increasing interests from the researchers in the fields of wastewater treatment and material science.

In this paper, the state-of-the-art of MOF-derivatives for adsorption, photoreduction and catalytic reduction toward Cr(VI) are summarized and listed in Table 1. MOFs-derived metal oxides and metal sulfides materials (like ZnS, In_2S_3, ZnO and Fe_2O_3), porous carbon materials (like Ni@carbon, $Fe_{0.72}^{(0)}Fe_{2.28}^{(II)}C$, Cu-carbon, nZVI@C), and some corresponding composite materials (like NZVI@ZD, PANI@NC-600) are discussed in detail. The involved reaction mechanisms and the influence factors toward Cr(VI) removal performances are demonstrated in Scheme 1. Finally, the challenges and prospects of MOF-derivatives for Cr(VI) removal are proposed and clarified.

2. Adsorptive removal

Adsorption has aroused wide attention due to the great availability of low-cost adsorbents, easy operation and high efficiency. In recent years, various adsorbents like activated carbon [87], lignocellulosic materials [88] and inorganic materials [89] are developed to achieve Cr (VI) adsorption. However, the relatively small specific surface area and large pores could inhibit the Cr(VI) removal efficiency. Some MOF-derived porous metal oxides and metal sulfides, porous carbon materials and layered materials with large specific surface area and adsorption active sites are favorable for Cr(VI) adsorption [90,91].

2.1. Metal oxides and their composites

Maghemite (γ-Fe_2O_3), obtained from the oxidation of diagenetic magnetite, is one of the naturally existing iron oxides, which can be commonly found in tropical and subtropical soils [92,93]. γ-Fe_2O_3 demonstrates some excellent merits like low-cost production, environment-friendly properties, magnetic characteristic and difficult to corrosion [94]. Many γ-Fe_2O_3 nanostructures like nanorods and nanowires have been investigated [95,96], which have aroused wide interest in adsorption [97,98].

It was deemed that enhancing specific surface area and/or functional groups of the adsorbents can accomplish boosted adsorption performances. Wen and co-workers [74] facilely prepared porous Fe_2O_3 (P-Fe_2O_3) microcubes with large specific surface area (155 $m^2\ g^{-1}$) and abundant Fe_2O_3 nanoparticles by annealing Prussian blue (PB) microcubes at 350 ℃. According to PXRD and selected area electron diffraction (SEAD) results, the obtained P-Fe_2O_3 microcubes were built up of cubic spinel γ-Fe_2O_3 nanoparticles, which were further confirmed by SEM and TEM images (Fig. 2b and 2c). It is well-known that the surface charge exert great effect on the adsorption performance [99]. The pH value of the zero-charge point of P-Fe_2O_3 was 7.2 (Fig. 2d). At pH < 7.2, the surface charge of P-Fe_2O_3 was positive because of the protonation of the oxygen-containing groups under acidic environment. On the contrary, the functional groups on the surface of P-Fe_2O_3 were deprotonated at pH > 7.2, which enable the surface charge of P-Fe_2O_3 to be negative [100]. Specific surface area and pore volume are important parameters to assess the adsorption capacity of adsorbent [101]. The prepared P-Fe_2O_3 showed a larger specific surface area (155 $m^2\ g^{-1}$) than those of both commercial α-Fe_2O_3 (17 $m^2\ g^{-1}$) and Prussian blue (3.7 $m^2\ g^{-1}$). The inherited porous framework and large surface area of the P-Fe_2O_3 will facilitate the transport of pollutants to the internal voids. The maximum Cr(VI) adsorption capacity over P-Fe_2O_3 was 175.5 mg g^{-1} at pH = 5.0 (Fig. 2e). The adsorption process of P-Fe_2O_3 toward Cr(VI) was spontaneous (ΔG^o (Gibbs free energy change) values (−3.55 kJ mol^{-1} at 298 K, −3.82 kJ mol^{-1} at 313 K, and −4.16 kJ mol^{-1} at 328 K)), endothermic (ΔH^o (standard enthalpy change) = 2.56 kJ mol^{-1}) and entropy increment (ΔS^o (standard entropy change) = 22.4 J mol^{-1} K^{-1}). When pH < 7.2, the existed $HCrO_4^-$ and CrO_4^{2-} were inclined to bind with P-Fe_2O_3 because of the electrostatic interactions. The adsorption capacity of P-Fe_2O_3 toward Cr (VI) decreased with the increase of pH, which can be assigned to the declined electrostatic attractions. The ion exchange between hydroxyl groups on the surface of P-Fe_2O_3 and Cr(VI) ions was also accountable for Cr(VI) adsorption [102,103]. The adsorption mechanism was confirmed by EDX elemental mapping and XPS analysis. The EDX

Table 1
The Cr(VI) removal performance of MOFs derivatives and their composites.

Derivatives	MOF precursors	Removal methods	Cr(VI) adsorption capacity (mg g^{-1})/reduction efficiency (%)	Initial concentration (mg L^{-1})	pH	Time (min)	Ref
P-Fe_2O_3	MOFs(Fe)	Adsorption	175.5*	10–80	5	–	[74]
Ni/Co-LDH	ZIF-67	Adsorption	99.9*	10–80	–	–	[75]
PANI@NC-600	UiO-66	Adsorption	198.04*	40–160	1	480	[76]
nZVI@C	MIL-100(Fe)	Adsorption and reduction	206*	–	3	1440	[77]
$Fe_{0.72}^{(0)}Fe_{2.28}^{(II)}C$	Fe-MOFs	Adsorption and reduction	354.6*	30–80	2	120	[78]
NZVI@ZD	ZIF-67	Adsorption and reduction	226.5*	5–600	5	180	[79]
ZnS	ZIF-L	Photoreduction	100**	20	4	30	[80]
In_2S_3	MIL-68	Photoreduction	100**	10	6	15	[81]
ZnO	HUT-11, HUT-12	Photoreduction	100**	10	–	120	[82]
Cu@C-550	HKUST-1	Catalytic reduction	100**	200	–	15	[83]
Ni@carbon 450	Ni-MOF	Catalytic reduction	100**	100	2	30	[84]
Ni@N-CNTs/N-G-800	Ni-MIL	Catalytic reduction	99.6**	50	–	50	[85]
PdCu/NCG	ZIF-8	Catalytic reduction	100**	130	2	7	[86]

Note: HUT-11, HUT-12: Zn-MOFs ($[Zn_5(\mu_3\text{-}OH)(BTC)_3(Phen)_4]\cdot 5H_2O$: HUT-11 and $[Zn_4(\mu 4\text{-}O)(BTC)_2(phen)_2]\cdot 4H_2O\cdot 4H_2O$: HUT-12)
BTC = 1,3,5-benzenetricarboxylic acid, phen = 1,10-phenanthroline; HKUST-1(Cu): Cu_3BTC_2; NZVI@ZD: NZVI@derivative of ZIF-67 (ZD); Ni@N-CNTs/N-G-800: Ni@N-doped graphene-CNT frameworks pyrolyzed at 800 ℃; Ni/Co-LDH: Ni/Co-layered double hydroxide; PdCu/NCG: PdCu/N-doped carbon/graphene
* Cr(VI) adsorption capacity (mg g^{-1}); ** Cr(VI) reduction efficiency (%)

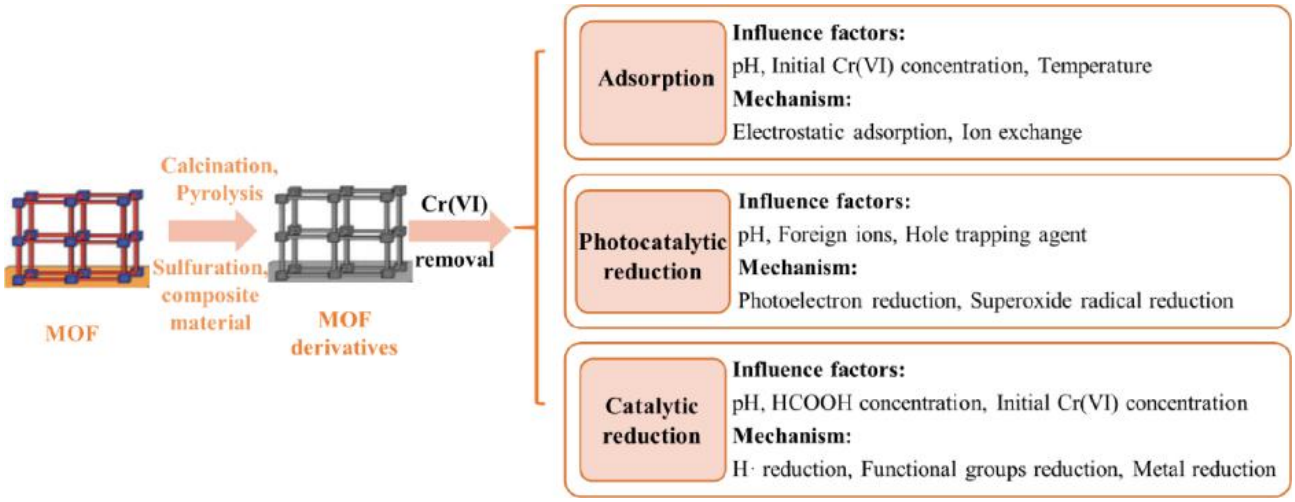

Scheme 1. Cr(VI) removal with MOF-derivatives and their composites.

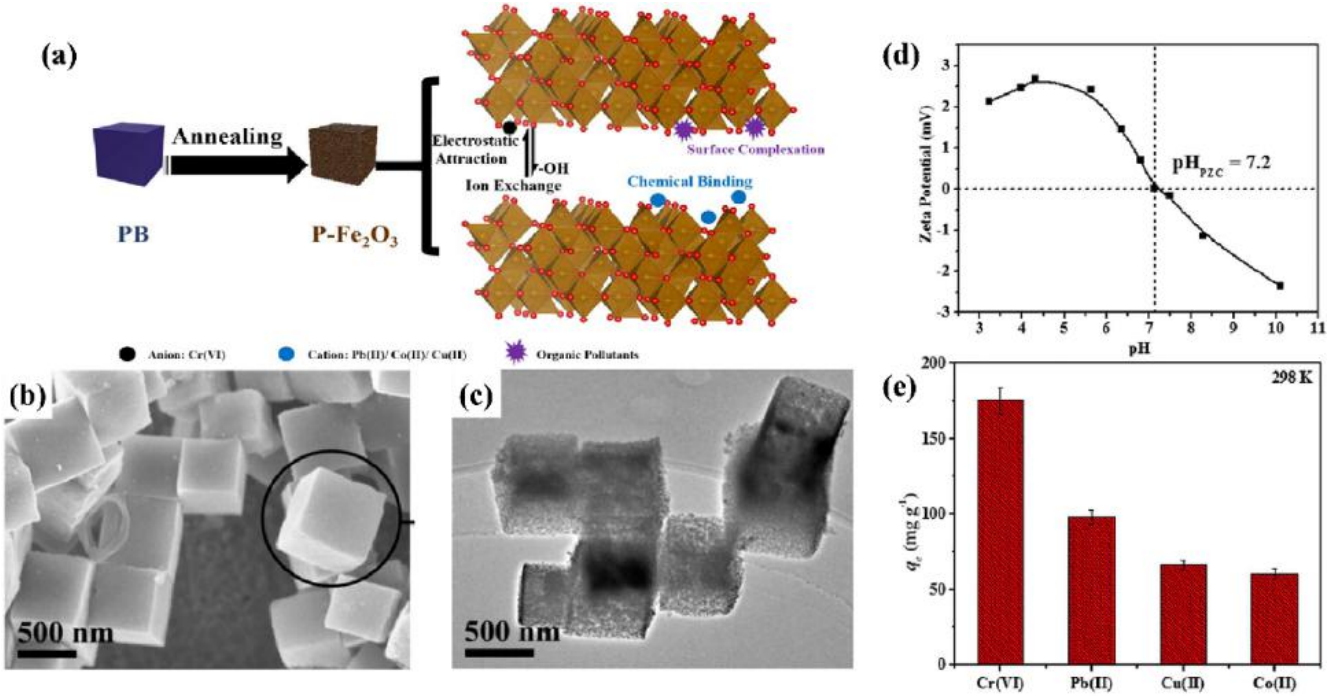

Fig. 2. Synthetic process and proposed reaction mechanism toward Cr(VI) adsorption (a); SEM (b) and TEM (c) image of P-Fe_2O_3. The zeta potential of P-Fe_2O_3 under different pH values (d); The adsorption capacities toward Cr(VI), Pb(II), Cu(II) and Co(II) over P-Fe_2O_3 [74].

elemental mappings demonstrated the distribution of Fe, O, Cr after adsorption and stability of P-Fe_2O_3 microcubes. In XPS analysis, the peaks of FeO_6 at 529.9 eV shifted to 530.1 eV as the result of the formation of Cr-O after adsorption. In addition, the reduction of Cr(VI) to Cr(III) did not occur during Cr(VI) adsorption on nano-maghemite [104,105]. Except for Cr(VI) adsorption, P-Fe_2O_3 also achieved elimination of metal cations (Pb(II), Cu(II) and Co(II)) and organic pollutants (MB, humic acid (HA), rhodamine B (RhB), and methyl orange (MO)) from aqueous solutions. This work facilely fabricated low-cost and easily available P-Fe_2O_3 from PB microcubes for pollutants removal, which provided a significant strategy to obtain inexpensive MOF derivatives for water purification in natural environment.

Recently, layered double hydroxides (LDHs), with layered structure as well as large surface area and ion exchange capacity, have been developed as the potential adsorbents [106–108]. Cheng and coworkers [75] prepared dodecahedral Ni/Co-layered double hydroxide (NiCo-LDH) by mixing $Ni(NO_3)_2$ with ZIF-67 and being ultrasonicated for 45 min (Fig. 3a). The formation mechanism of NiCo-LDH could be described as: Ni^{2+} ions can be hydrolyzed to produce protons when Ni $(NO_3)_2$ was mixed with the ethanol suspension of ZIF-67. The formed protons could corrode ZIF-67 and promote NO_3^- oxidation under acid condition. Then, the Co^{2+} in ZIF-67 was oxidized to Co^{3+} because of its lower reduction potential. Subsequently, the OH^- ions increased as the H^+ ions were consumed, which enabled the coprecipitates of divalent and trivalent metal ions around ZIF-67 to form LDH layer on the surface of ZIF-67. The inner structure of ZIF-67 gradually collapsed as the reaction went on to yield hollow dodecahedral structure [109].

The results of adsorption kinetics experiments revealed higher removal efficiencies for adsorbing Cr(VI) than $NiCo_2O_4$-NiO (NiCo-LDH calculated at 350 °C), and the adsorption isotherms experiments demonstrated the Cr(VI) adsorption fitted with Langmuir model. The zeta potential values of $NiCo_2O_4$-NiO and NiCo-LDH were determined as

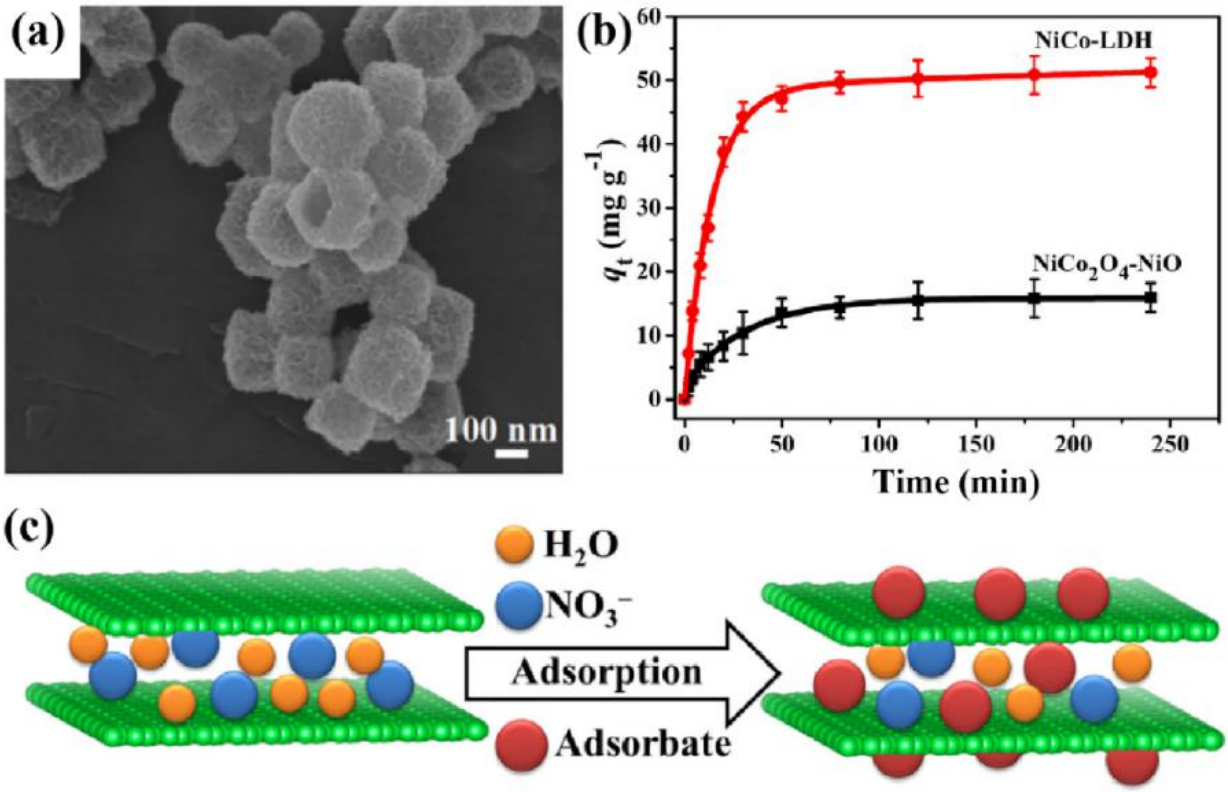

Fig. 3. SEM image of NiCo-LDH (a); Adsorption capacity of NiCo-LDH and $NiCo_2O_4$-NiO changes with different times (b); The adsorption mechanism of NiCo-LDH (c) [75].

23.6 and 16.8 mV at pH = 7, respectively, which indicated the electrostatic attraction between Cr(VI) and the prepared NiCo-LDH. Although the zeta potential showed that the surface charge of NiCo-LDH was slightly less positive than $NiCo_2O_4$-NiO, NiCo-LDH exhibited larger Cr(VI) adsorption capacity (99.9 mg g^{-1}) according to the calculation of Langmuir model, due to the larger SBET (267 m^2 g^{-1}) and layered porous nanostructures (Fig. 3b). After five cycles, adsorption efficiencies toward Cr(VI) declined from 91.6% to 67.5%. In the FTIR spectrum, NiCo-LDH has a strong band at 1385 cm^{-1}, which corresponded to the N-O vibrational peak of NO_3^-. However, this typical peak decreased significantly after adsorption, indicating that some NO_3^- ions in the NiCo-LDH layers might be substituted by Cr(VI) ions. Therefore, the mechanism was speculated that Cr(VI) adsorption over NiCo-LDH was mainly ascribed to electrostatic interaction and ion exchange (Fig. 3c). Besides Cr(VI), NiCo-LDH can also accomplish efficient adsorption toward anionic organic pollutants like Congo red (CR), which can be potentially adopted to achieve effective removal toward pollutants with negative charge. The fabrication of NiCo-LDH provided a design methodology for adsorbents and enhanced removal efficiency for anionic organic pollutants as well as Cr(VI) ions.

2.2. PANI/N-doped carbon nanoparticles

As a conductive polymer, polyaniline (PANI) has been investigated for Cr(VI) reduction due to the rich reductive amine groups and oxidative imine groups [110,111]. In addition, PANI displays great stability under the acidic condition, which further benefits for Cr(VI) removal. Among different Zr-based MOFs, UiO-66 is a cubic porous MOF based on $Zr_6O_4(OH)_4$ nodes and 1,4-benzodicarboxylates [112]. Some merits like aqueous stability, low-cost production, and large specific surface area enable UiO-66 to be a promising precursor [113–115]. Zhang and co-workers [76] prepared N-doped carbon nanoparticles (NC) using UiO-66 as a template, and then polyaniline (PANI) was introduced to modify NC by in-situ polymerization (Fig. 4a and 4b). The surface area of NC-600 (being treated at 600 °C) was 1609.1 m^2 g^{-1}, much larger than those of NC treated at 400 °C, 800 °C and 1000 °C, as well as commercially activated carbon (990.8 m^2 g^{-1}). NC-600 also demonstrated the largest *meso*-porosity, which may be conductive for pollutant adsorption. After modified by PANI, the specific surface area of PANI@NC-600 can still be 600.8 m^2 g^{-1}, which was higher than pristine UiO-66 and PANI. When pH = 1, the adsorption efficiency toward Cr(VI) was up to 99%, and the calculated maximum adsorption capacity reaches 198.04 mg g^{-1} (Fig. 4c and 4d). After 5 cycles, the Cr (VI) removal efficiency was still maintained at about 84.52%, and the adsorption capacity can also reach 169.04 mg g^{-1}. The mechanisms of PANI@NC-600 to remove Cr(VI) were proposed as two steps: (i) Cr(VI) ions quickly diffused to the surface of PANI@NC-600 and then were adsorbed on the protonated sublayer; (ii) Cr(VI) ions could react with the amine groups of PANI and be reduced into less toxic Cr(III) ions, which were also adsorbed on the surface of PANI@NC-600 and chelated with the imino groups (Fig. 4e). The successful construction of PANI/N-doped carbon nanoparticles and the superior adsorption capacity afford novel insight into the composites of MOF derivatives and the benefits of modification.

2.3. Fe-based carbon materials and their composites

So far, various Fe-based materials like zero-valent iron, ferrites, and iron-based metallic glasses have been proven to be effective adsorbents and catalysts for pollutants removal [116–119]. Considering their merits like easy separation with the aid of magnetic field, facile preparation and abundant active sites, both Fe(II) and Fe(0) have been used as Cr(VI) reduction agents [120,121]. In recent years, direct calcination or pyrolysis of MOFs (without using any additional carbon source) have been used to prepare MOF derived metals or metal oxide/carbon composites. Fe-MOF derived porous carbon materials can

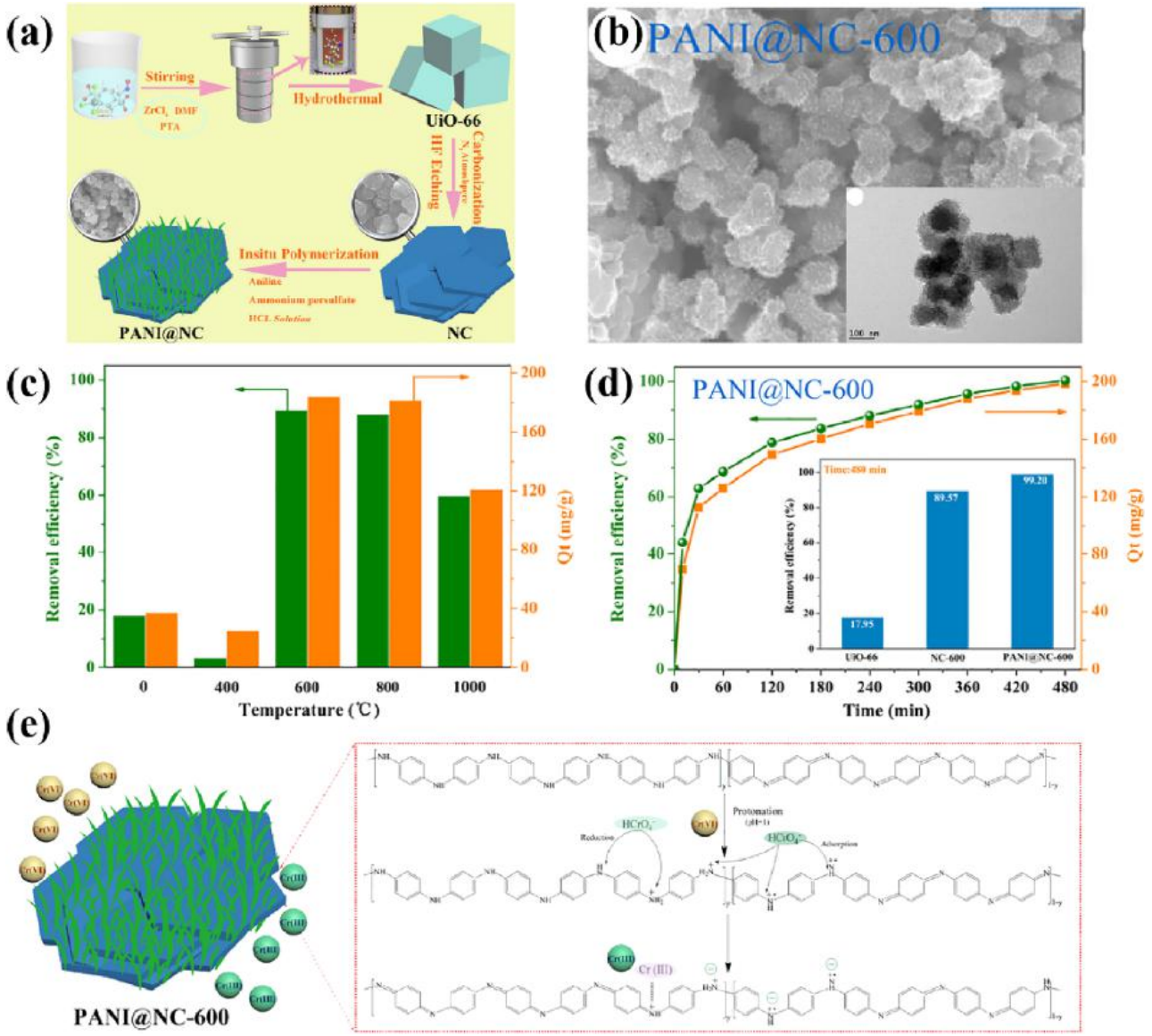

Fig. 4. SEM (a) and TEM (b) images of PANI@NC-600; The different Cr(VI) removal performances of various adsorbents (c); the performance of PANI@NC-600 toward Cr(VI) removal and removal rate by UiO-66, NC-600, and PANI@NC-600 at 480 min (d); The mechanism of Cr(VI) removal by PANI@NC-600 (e) [76].

combine the advantages of Fe-based materials with carbon materials, which can promote the Cr(VI) removal ability. The Cr(VI) ions with low concentration can be concentrated via the high adsorption capacity of carbon materials, which can be subsequently reduced to Cr(III) by the iron species in Fe-doped carbon material.

2.3.1. *Pristine porous carbon derived from Fe-MOFs*

To overcome the poor physicochemical properties like lower specific area and aggregation of conventional Fe_3O_4 and other Fe-based NPs, Yang and co-workers [78] synthesized Fe-MOF derived porous $Fe_{0.72}^{(0)}Fe_{2.28}^{(II)}C$ in vacuum or under N_2 atmosphere at 750 ℃ for 4 h, in which the formation of Fe with low valence like Fe(0) and Fe(II) could be conductive to achieve higher efficiencies [122]. A uniform spindle-like shape of $Fe_{0.72}^{(0)}Fe_{2.28}^{(II)}C$ was observed in SEM images (Fig. 5a), and HRTEM image also displayed nanoparticles coated with graphitized carbon [123]. The specific surface area of $Fe_{0.72}^{(0)}Fe_{2.28}^{(II)}C$ (100.42 $m^2\ g^{-1}$) was higher than that of Fe-MOF (62.70 $m^2\ g^{-1}$). The vibrating sample magnetometer (VSM) analysis confirmed ferromagnetic behavior of $Fe_{0.72}^{(0)}Fe_{2.28}^{(II)}C$ with a larger saturation magnetization of 90.7 emu g^{-1}.

When pH = 2, the maximum adsorption capacity of $Fe_{0.72}^{(0)}Fe_{2.28}^{(II)}C$ toward Cr(VI) was 354.6 mg g^{-1}. With the initial pH value increasing, the maximum adsorption amount of Cr(VI) gradually decreased (Fig. 5b). Under the acidic conditions, the surface of $Fe_{0.72}^{(0)}Fe_{2.28}^{(II)}C$ underwent a deprotonation reaction to be positively charged, which further enhanced the Cr(VI) adsorption via the electrostatic interactions. The kinetic and isotherm investigations on Cr(VI) removal illustrated that Cr(VI) adsorption process was ascribed to pseudo-second-order kinetic model and was well fitted with Langmuir model [124], with the calculated maximum adsorption amount being 354.6 mg g^{-1}. The Cr(VI) adsorption ability of $Fe_{0.72}^{(0)}Fe_{2.28}^{(II)}C$ decreased slightly in tap water and surface water due to the co-existence of low-content anions and organics. However, it is worth noting that Cr(VI) removal capacity in chemical oxygen demand sample wastewater produced by laboratory containing H_2SO_4, Ag_2SO_4, $HgSO_4$, and $K_2Cr_2O_7$ increased to 336.7 mg g^{-1}. According to XRD analysis, $HgCrO_4$ and $Ag_2Cr_2O_7$ formed by reaction between Hg^{2+}, Ag^+ and $Cr_2O_7^{2-}$, $HCrO_4^-$ were adsorbed onto $Fe_{0.72}^{(0)}Fe_{2.28}^{(II)}C$, which contributed to the efficient Cr(VI) removal.

In order to explore the reusability, $Fe_{0.72}^{(0)}Fe_{2.28}^{(II)}C$ was treated and recovered with 1 M NaOH and magnetic field. Considering that the

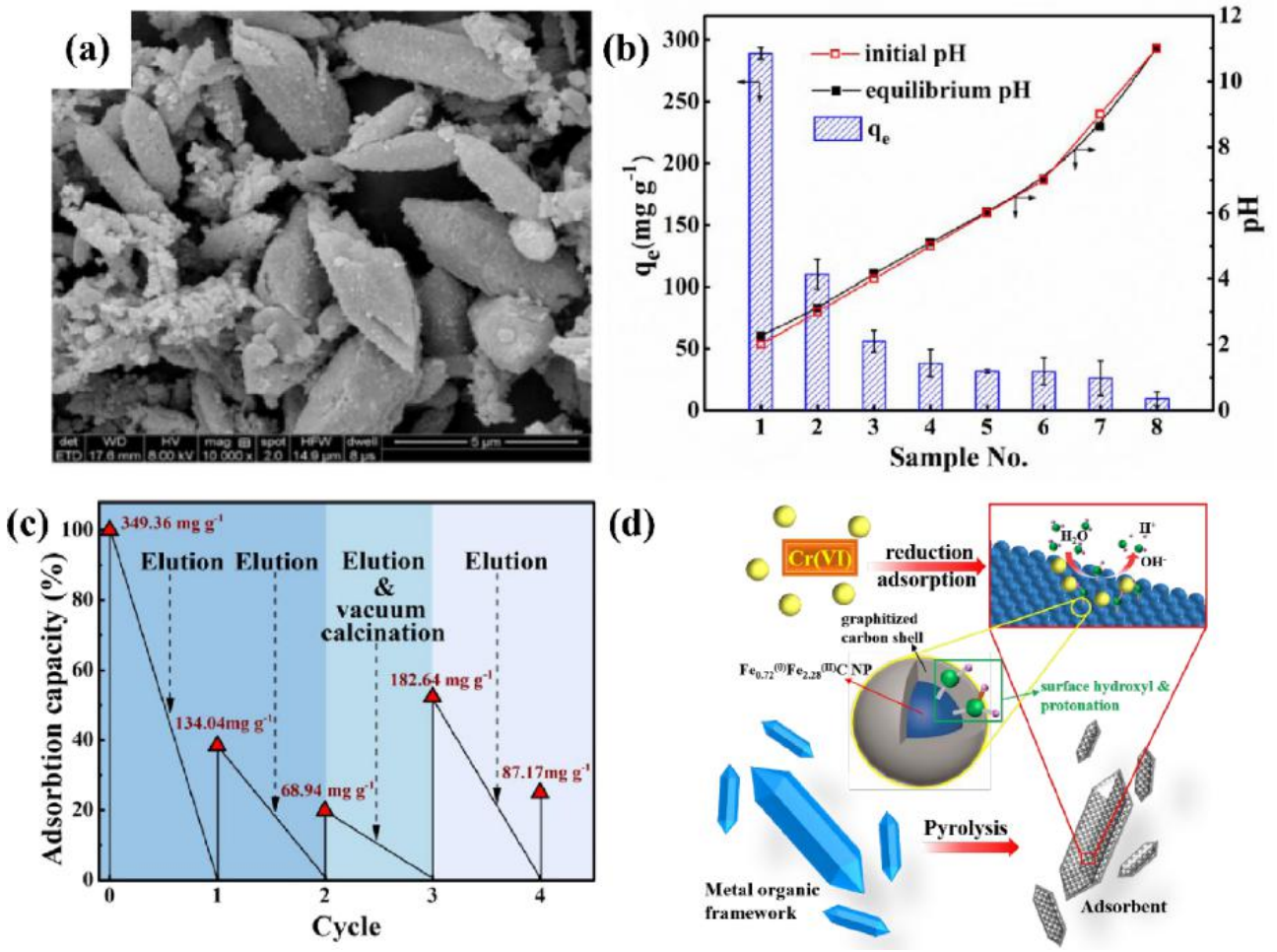

Fig. 5. SEM image of $Fe_{0.72}^{(0)}Fe_{2.28}^{(II)}C$ (a); Effect of initial pH values on Cr(VI) removal (b); The cyclic performance of $Fe_{0.72}^{(0)}Fe_{2.28}^{(II)}C$ (c); Cr(VI) removal mechanism over $Fe_{0.72}^{(0)}Fe_{2.28}^{(II)}C$ [78].

Cr(VI) removal capacity decreased with each successive cycle (Fig. 5c), besides being treated with NaOH, calcination under vacuum at 750 °C was adopted to maintain the adsorption performance. In the third cycle, $Fe_{0.72}^{(0)}Fe_{2.28}^{(II)}C$ was both eluted with NaOH and calcined under vacuum at 750 °C to resume the adsorption capacity, in which the adsorption capacity after third cycle still reached 182.64 mg g^{-1}, much higher than that only generated with NaOH. On the basis of XPS results, it was found that Cr(VI) and Cr(III) exist on the surface of $Fe_{0.72}^{(0)}Fe_{2.28}^{(II)}C$ after adsorption, which demonstrated that part of the adsorbed Cr(VI) was reduced to lower toxic Cr(III) in the process of adsorption. Therefore, the possible mechanism for Cr(VI) removal from water could be proposed: Cr(VI) was firstly adsorbed on the $Fe_{0.72}^{(0)}Fe_{2.28}^{(II)}C$ via electrostatic interaction (Fig. 5d). Partial Fe(0) and Fe(II) in the $Fe_{0.72}^{(0)}Fe_{2.28}^{(II)}C$ can convert Cr(VI) to Cr(III) via reduction reaction, which were further oxidized to Fe(III). At the same time, OH^- was generated, causing an increase in pH and produced $Cr(OH)_3$ precipitates (Eqs. 1–7). This work affords a strategy for preparing Fe-containing carbon adsorbents with MOFs as precursor via calcination to achieve efficient Cr(VI) adsorption and chemical reduction by Fe(0) and Fe(II) inside the structure.

$$H_2O \leftrightarrow H^+ + OH^- \quad (1)$$

$$Fe^{(0)} \rightarrow Fe^{(II)} \rightarrow Fe^{(III)} \quad (2)$$

$$2Fe^{(0)} + Cr_2O_7^{2-} + 7H^+ \rightarrow 2Cr^{(III)} + 2Fe^{(III)} + 7OH^- \quad (3)$$

$$6Fe^{(II)} + Cr_2O_7^{2-} + 7H^+ \rightarrow 2Cr^{(III)} + 6Fe^{(III)} + 7OH^- \quad (4)$$

$$Fe^{(0)} + HCrO_4^{2-} + 3H^+ \rightarrow Cr^{(III)} + Fe^{(III)} + 4OH^- \quad (5)$$

$$3Fe^{(II)} + HCrO_4^{2-} + 3H^+ \rightarrow Cr^{(III)} + 3Fe^{(III)} + 4OH^- \quad (6)$$

$$Cr^{(III)} + 3OH^- \rightarrow Cr(OH)_3 \quad (7)$$

Considering that the traditional nZVI-encapsulated carbon (nZVI@carbon) adsorbents usually suffered from the drawbacks like low Fe content, being easily oxidized, easy aggregation and small specific surface area [125], Gu and co-workers [126] adopted MIL-100(Fe) as template to prepare nZVI@C by one-step carbothermal reduction. The abundant ordered Fe-O clusters in MIL-100(Fe) can achieve the high content and uniform distribution of nZVI in porous carbon skeleton with large specific surface area. The size of encapsulated nZVI can be regulated by different pyrolysis temperatures from 700 to 900 °C. Due to the well-controllable morphology of carbon framework and suitable size of magnetic particles, the as-prepared Fe@C-800 (carbonization temperature at 800 °C) displayed best adsorption capacity toward Cr (VI) (206 mg g^{-1}) (Fig. 6d). The surface charge of Fe@C-800 was positive due to the protonation reaction at pH < 5.12 (Fig. 6c), and the surface of Fe@C-800 changed from positively charged to negatively charged as the pH values increased. The mechanism of removing Cr(VI) from water over Fe@C-800 was comparable to that of $Fe_{0.72}^{(0)}Fe_{2.28}^{(II)}C$. The anionic Cr(VI) ions were adsorbed on the positive surface of Fe@C-800 with the aid of the electrostatic interactions, and

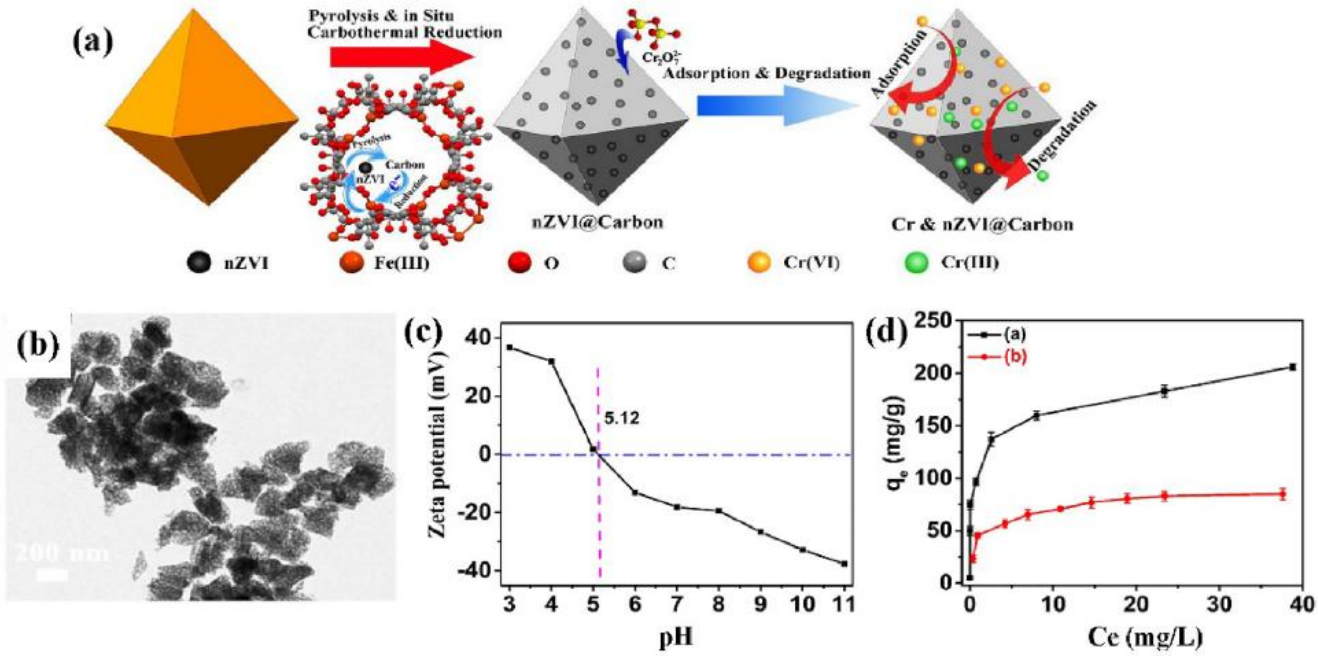

Fig. 6. Synthetic process and proposed reaction mechanism toward Cr(VI) removal (a); TEM image of Fe@C-800 (b); Zeta potentials of Fe@C-800 at different pH values (c); Adsorption isotherm of Fe@C-800 and C-800 for the Cr(VI) adsorption (d) [126].

some adsorbed Cr(VI) ions were reduced into Cr(III) to yield $Cr(OH)_3$ precipitates. This work highlighted the Cr(VI) adsorption and in-situ reduction over Fe@C-800 by converting nZVI to Fe_2O_3 were achieved without the addition of the electron donor acid.

2.3.2. NZVI/MOFs derivatives

Nanoscale zero-valent iron (NZVI) was one of the promising materials for Cr(VI) removal [127]. As well, the carbonized derivatives of zeolitic imidazole framework-67 (ZIF-67) with zeolite-type pore structure could maintain the unique characteristics of MOFs and generate larger pore size. Wen and co-workers [79] prepared NZVI and porous core–shell carbon composite NZVI@ZD (the derivative of ZIF-67) through carbonization with core–shell structure NZVI@ZIF-67 as a precursor (Fig. 7a). In detail, the NZVI was mixed with the organic ligand 2-methylimidazole, then NZVI@ZIF-67 was obtained by in situ reaction at room temperature. NZVI@ZD was synthesized after carbonizing under a nitrogen flow at 800 ℃ for 2 h. NZVI@ZD exhibited highly porous structure and large specific surface area (254.5 $m^2\ g^{-1}$). Both the formed Co nanoparticles in the composites and the encapsulated NZVI exhibited good dispersibility in the carbon substrate, in which the existence of NZVI made the NZVI@ZD display high magnetic properties. In addition, the transformation of the carbonized NZVI@ZD from micropores to mesopores was achieved through carbonization.

The maximum adsorption capacity of NZVI@ZD toward Cr(VI) was calculated as 226.5 mg g^{-1} via Langmuir isothermal model, which was larger than that of NZVI@ZIF-67 (36.53 mg g^{-1}). The pH values of the Cr(VI) solution exerted significant influence on the adsorption capacity of NZVI@ZD, in which the removal efficiency under acidic condition was higher than that in alkaline environment (Fig. 7b). Under acidic conditions, the positive zeta potential of NZVI@ZD enhanced the adsorptive interactions toward anionic Cr(VI). The Cr(VI) removal mechanism was proposed in Fig. 7d. It was known that the size of Cr(VI) ($Cr_2O_7^{2-}$) is ca. 7.5 Å [128], which could be adsorbed into mesoporous ZD shell and gradually entered the interior structure through electrostatic interaction. The contact between NZVI core and Cr(VI) induced the Cr(VI) reduction into Cr(III) to form $Cr(OH)_3$ (Fig. 7c). Additionally, ZD-rich pores can also provide the abundant active sites, which corresponded to the increased both reduction rate and efficiency. In this study, the magnetic NZVI@ZD can encapsulate the adsorbed Cr(VI) and the formed Cr(III) to achieve the efficient total chromium removal in water and easy separation from solution.

3. Photocatalytic reduction

It was reported that the pH value, Cr(VI) concentration and the redox potential can exert significant impacts on the relative distribution of Cr(VI) species including $Cr_2O_7^{2-}$, CrO_4^{2-}, H_2CrO_4, and $HCrO_4^-$ [129]. Direct precipitation is not feasible to separate Cr(VI) species from solution due to their solubility [6]. However, Cr(III) could form insoluble $Cr(OH)_3$ under high pH values. Therefore, changing the oxidation state and converting the high-toxic Cr(VI) to low-toxic Cr(III) are deemed as the effective decontamination processes. Among the various methods of Cr(VI) reduction like chemical, electrochemical and biological methods [6], photocatalytic reduction of Cr(VI) to Cr(III) is effective, low-cost and environmentally friendly and free producing additional hazardous materials [130–132]. Photocatalysis on semiconductors is accompanied by the generation of photo-induced electron (e^-) - hole (h^+) pairs and charge separation. Therefore, photocatalytic oxidation of organic matter could also be achieved simultaneously during the photoreduction reaction, due to that organic matter serves as electron donor and hole capture agent [133,134].

Up to now, some traditional semiconductor photocatalysts like TiO_2 [135,136], ZnS [137,138], ZnO [139,140], In_2S_3 [141], along with other metal oxides/sulfides [142,143] have achieved photocatalytic Cr (VI) reduction from wastewater. However, the photocatalysts prepared via traditional methods suffered from small specific surface area (SSA) and low photocatalytic efficiency, which exerted limit to their applications in water treatment processes. The above-stated semiconductor photocatalysts with large SSA and abundant porosity could be prepared with porous MOFs as precursors [144–146], which can facilitate the concentration and transfer of pollutants to the photocatalytic active sites for enhanced photocatalytic reactions [147].

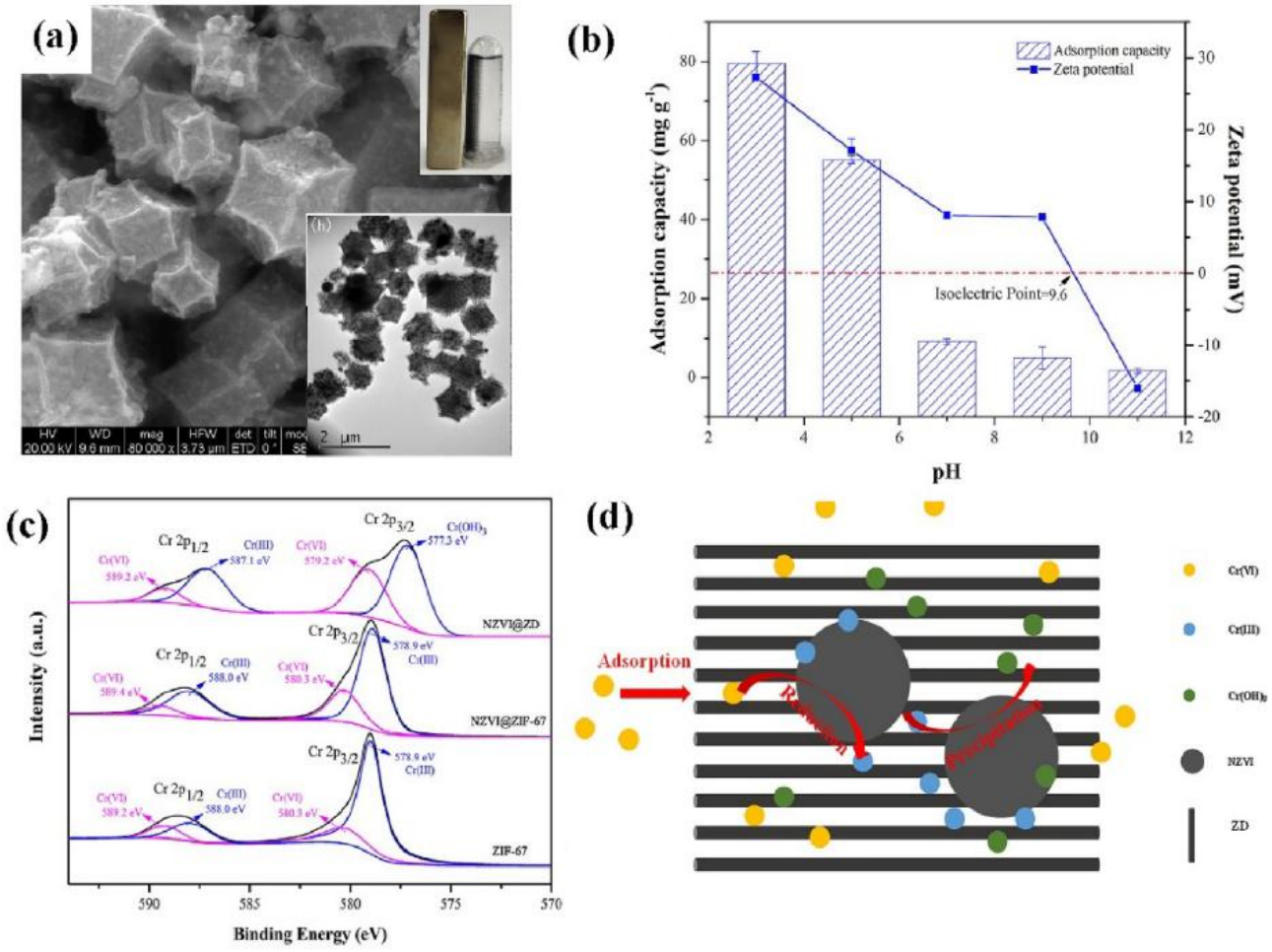

Fig. 7. SEM and TEM image of NZVI@ZD (a); The Cr(VI) adsorption capacity and zeta potential of NZVI@ZD under different pH values (b); Cr 2p XPS spectra of ZIF-67, NZVI@ZIF-67 and NZVI@ZD after adsorption (c); the proposed mechanisms of Cr(VI) removal over NZVI@ZD (d) [79].

3.1. Metal sulfides

As a major form of minerals, metal sulfides with variety of structural types provide wide field for exploration. Abundant and cheap metal sulfides like Ni_3S_2, Cu_2S and FeS_2 usually exist as minerals under natural conditions [148]. Many metal sulfides semiconductors have been obtained to develop light-sensitive photocatalysts, such as CdZnS [149], CuS [150], ZnS [151], and Bi_2S_3 [152].

ZnS, as a semiconductor photocatalyst with wide bandgap (E_g = 3.7 eV), has been adopted to carry out photocatalytic pollutant elimination from wastewater, considering that ZnS is stable, easily available, and nontoxic. ZnS with various morphologies like nanoparticles, nanowires, hollow nanosphere and nanotubes displayed outstanding photocatalytic Cr(VI) reduction activities [153]. Some strategies like thermal decomposition [154], solvothermal method [155], thermal evaporation method [156], and chemical precipitation method [157] were introduced to obtain the ZnS with different morphologies, which suffered from either high temperature or high pressure or both of them. It was essential to find a facile method to fabricate desired ZnS with both special structures and superior photocatalysis activity.

Our group synthesized rod-like ZIF-L (ZIF-R) from 2-methylimidazole (mim) and Zn^{2+} with the presence of polyvinylpyrrolidone (PVP) [158]. Subsequently, our group further prepared hollow ZnO nanotubes and used them to achieve efficient sensing detect toward acetone [159]. Encouraged by our previous work, we recently [80] produced porous tube-like ZnS by sulfurizing the as-prepared ZIF-R with thioacetamide (TAA) (Fig. 8a and 8b). The formation of porous ZnS tubes in this process could be described as the following: (i) the S^{2-} ions released from the hydrolysis of TAA reacted competitively with Zn^{2+} in form of coordinative Zn-N bond over the surface of ZIF-R to yield ZnS with the help of PVP; (ii) the 2-mim inside ZIF-R was stepwise replaced by the released S^{2-} to form porous ZnS structure as the inside Zn^{2+} could be diffused to outside [160]. The formation mechanism of porous tube-like ZS-X (ZnS formed by being sulfurized for different time) structure was affirmed by powder X-ray diffraction (PXRD), Fourier transform infrared spectroscopy (FTIR), and solid-state nuclear magnetic resonance spectroscopy (SSNMR) spectra. The UV–vis DRS spectra showed the light absorption edge of porous tubular ZnS could be extended to 400 nm, indicating that it can be excited by ultraviolet light. The porous ZS-3 (ZnS formed by being sulfurized for 3 h) displayed best photocatalytic Cr(VI) reduction performances under ultraviolet light, which was superior to both commercial TiO_2 (P25) and commercial ZnS (Fig. 8c). The electrochemical impedance spectroscopy (EIS) measurements affirmed that both P25 and commercial ZnS displayed smaller arc radius than ZS-3, implying that ZS-3 demonstrated higher separation efficiency of photogenerated charge carriers [161]. To explore the optimal photocatalytic reaction conditions, the effects of pH and foreign ions on the photocatalytic activities were investigated. It was observed that better photocatalytic performances were accomplished under lower the pH value (Fig. 8d). In acidic solution, the main forms of Cr (VI) are $HCrO_4^-$ and $Cr_2O_7^{2-}$ [162]. The photocatalytic reactions are demonstrated in Eqs. (8) and (9) [163], in which the presence of abundant H^+ can promote the Cr(VI) photoreduction. In alkaline circumstance, CrO_4^{2-} is the primary form in solution [164,165], which

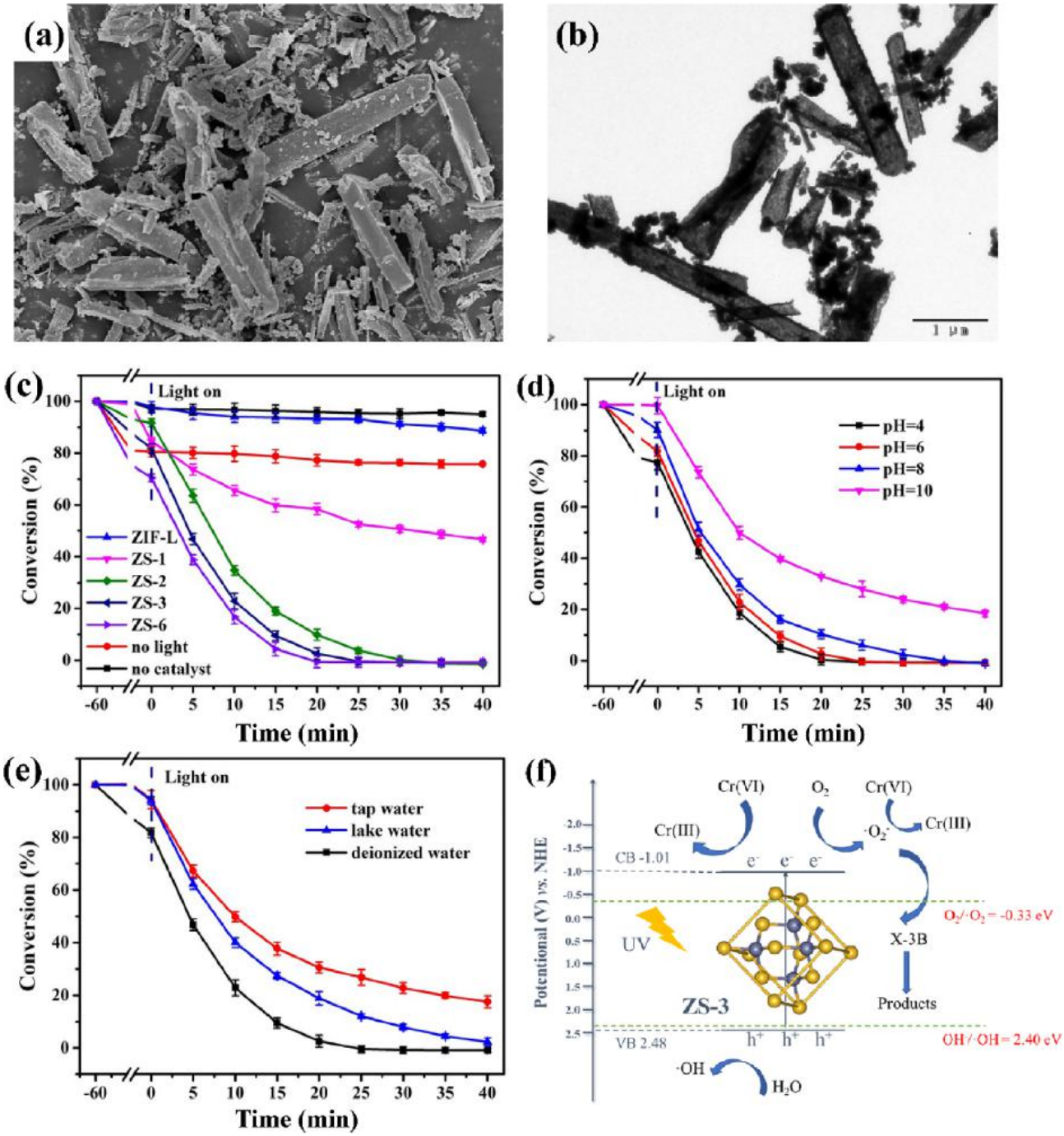

Fig. 8. SEM (a) and TEM (b) images of porous tube-like ZnS; The comparison of photocatalytic Cr(VI) reduction performances over ZIF-L and sulfurized products (c); Effect of pH values on Cr(VI) reduction performances (d); Effect of different water quality on Cr(VI) reduction (e); The proposed mechanism of photocatalytic Cr(VI) reduction over ZS-3 [80].

followed the chemical reactions of Eqs. (9) and (10) [163]. The formed $Cr(OH)_3$ at pH > 6 may cover the active sites of ZS-3 [134]. Furthermore, the decrease of zeta potential with the increased pH indicated the declined adsorption capacity toward Cr(VI) over ZS-3 at higher pH, which was not beneficial for the capture of photogenerated electrons to achieve photocatalytic Cr(VI) reduction. The photocatalytic Cr(VI) reduction efficiency was also influenced by foreign ions including inorganic salts and organic matter. The Cr(VI) solutions prepared from real lake water or tap water were treated by ZS-3. As shown in Fig. 8e, the Cr(VI) reduction efficiency for the simulated wastewater prepared from real tap water and lake water reached 82.5% and 97.8% within 40 min, respectively. The inorganic ions like K^+, Na^+, Ca^{2+}, Mg^{2+}, SO_4^{2-}, Cl^-, NO_3^- and PO_4^{3-} in tap water can inhibit the photocatalytic Cr(VI) reduction [166], causing a significant decline of Cr(VI) photoreduction efficiency. However, the presence of dissolved organic matter (DOM) will consume holes and facilitate the photocatalytic reaction [163]. Therefore, the higher Cr(VI) reduction efficiency in lake water was the result of the balanced effects of inorganic ions and organic matters.

$$14H^+ + Cr_2O_7^{2-} + 6e^- \rightarrow 2Cr^{3+} + 7H_2O \quad (8)$$

$$2H_2O + 2h^+ \rightarrow H_2O_2 + 2H^+ \quad (9)$$

$$CrO_4^{2-} + 4H_2O + 3e^- \rightarrow Cr(OH)_3(s) + 5OH^- \quad (10)$$

It has been widely explored that photocatalytic reduction and oxidation can be achieved simultaneously in the photocatalytic processes, due to that the photo-induced electrons are accompanied by the photo-generated holes [167,168]. Therefore, photocatalytic Cr(VI) reduction and organic pollutant (Reactive Red X-3B, X-3B) oxidation were investigated in aqueous solution. In the Cr(VI) and organic pollutant (X-3B) matrix, the Cr(VI) reduction efficiency decreased slightly and the photocatalytic X-3B oxidation efficiency decreased from 97.7% to 25.0% over ZS-3, which could be attributed to the competition of photo-induced electrons between the Cr(VI) reduction and the formation of $\cdot O_2^-$ (being participated in the oxidation of X-3B) (Fig. 8f) [169]. The Cr(VI) photoreduction efficiency maintained at 100.0% after three runs, indicating that ZS-3 exhibited good reusability, which was affirmed by PXRD, SEM and TEM of the used ZS-3. The prepared porous tube-like ZnS enriched the morphology of ZnS semiconductors and enhanced the performances of Cr(VI) photocatalytic reduction. This work provided a feasible strategy to fabricate metal sulfides with high photocatalytic efficiencies.

As another typical semiconductor sulfide, In_2S_3 has received extensive attentions in the optics, photoconduction and photoelectricity with bandgap of 2.0–2.2 eV [170]. Nanostructured In_2S_3 like nanotubes, nanorods and nanosheets exhibited great potential applications in photocatalytic reaction due to its superior properties like photosensitivity, photoconductivity, chemical stability and other physical characteristics [141,171,172].

Recently, our group successfully prepared rod-shaped MIL-68 using water or sodium salt as a regulator at the room temperature [81], which was beneficial to its high throughput production. Then, porous In_2S_3 (Fig. 9a and 9b) derived from rod-shaped MIL-68 was obtained by solvothermal method with the aid of thioacetamide. It can be seen from the UV–vis spectrum that the light absorption range of porous hollow In_2S_3 was extended to the visible light region, indicating that the porous In_2S_3 can be excited by visible light. The porous hollow In_2S_3 exhibited high photocatalytic Cr(VI) reduction efficiency at pH = 6.0 under 350 mW LED visible light irradiation, in which 10 mg L^{-1} of Cr(VI) can be completely removed within 15 min. Combining active species capture experiments and electron spin resonance (ESR) (Fig. 9c and 9d), the leading active species for reducing Cr(VI) were identified as e^- and $\cdot O_2^-$ (Fig. 9f) [173,174]. After five cycles, as shown in Fig. 9e, the photocatalytic reduction efficiency can still achieve 95% within 10 min, which demonstrated that the obtained In_2S_3 could be used for long-term operation. This work revealed that the metal sulfides with different morphologies can be regulated by the morphologies of the MOF precursors, which could exhibit higher photocatalytic Cr(VI) reduction performance.

3.2. Metal oxides

Metal oxide semiconductors display different characteristics from traditional inorganic semiconductors in charge transport mechanisms and optoelectronic properties, which capacitate them more functions [175]. Some metal oxides like TiO_2 with light absorption properties, capability of generating charge carriers, stability as well as biocompatibility can exhibit the photocatalytic activities once input the required amount of light energy [176]. Also, ZnO possesses a relatively wide band gap (3.3 eV), specific optoelectrical property, high electron mobility, as well as high chemical stability and thermal stability, which enables it to arise broad interest in photocatalysis [177]. However, some synthesizing techniques of ZnO including chemical and physical deposition usually generate products with low specific surface area and limited photocatalytic efficiency.

He and co-workers obtained nano-sized ZnO (ZnO-11 and ZnO-12) (Fig. 10b and 10c) by calcining two different Zn-MOFs ($[Zn_5(\mu3\text{-}OH)(BTC)_3(Phen)_4]\cdot 5H_2O$ (HUT-11) and $[Zn_4(\mu4\text{-}O)(BTC)_2(phen)_2]\cdot 4H_2O\cdot 4H_2O$ (HUT-12) [82] in muffle furnace at 600 °C (Fig. 10a). PXRD, FTIR spectra and TGA analysis confirmed the successful fabrication of Zn-MOFs and the nano-sized ZnO. As depicted in Fig. 10b and 3c, the synthesized ZnO presents oval and circular or hexagonal morphology, which could contribute to the potential possibilities of morphology adjustment. It can be noted that the size of ZnO-11 nanoparticles was in a broad range of 100–400 nm, while the particle size of ZnO-12 was relatively small (50 nm). The photocatalytic experiments results indicated that HUT-12 exhibited better Cr(VI) reduction performances than HUT-11, which may be attributed to the differences in the coordination atoms, coordination

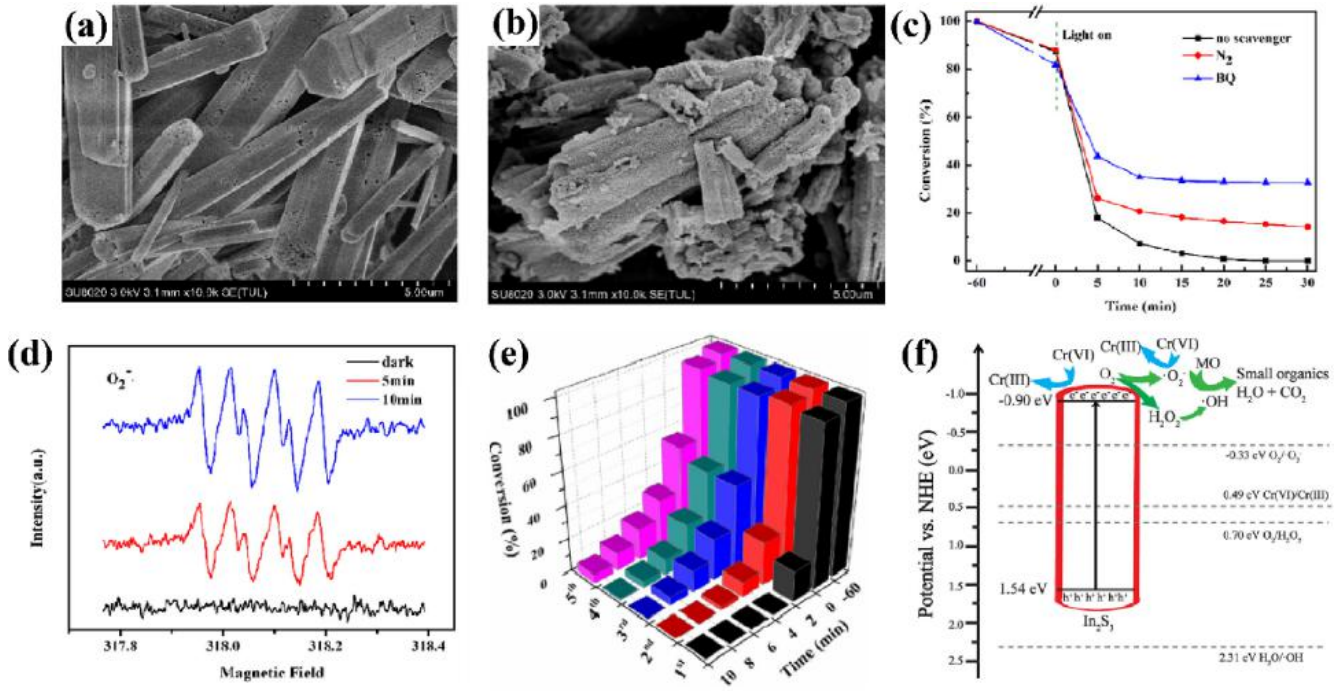

Fig. 9. SEM images of MIL-68 prepared with NaF (a) and In_2S_3 (b); Effects of different scavengers on Cr(VI) reduction (b); ESR spectra (c); Reusability for the Cr(VI) photoreduction (d); Proposed mechanism of Cr(VI) photoreduction (e) [81].

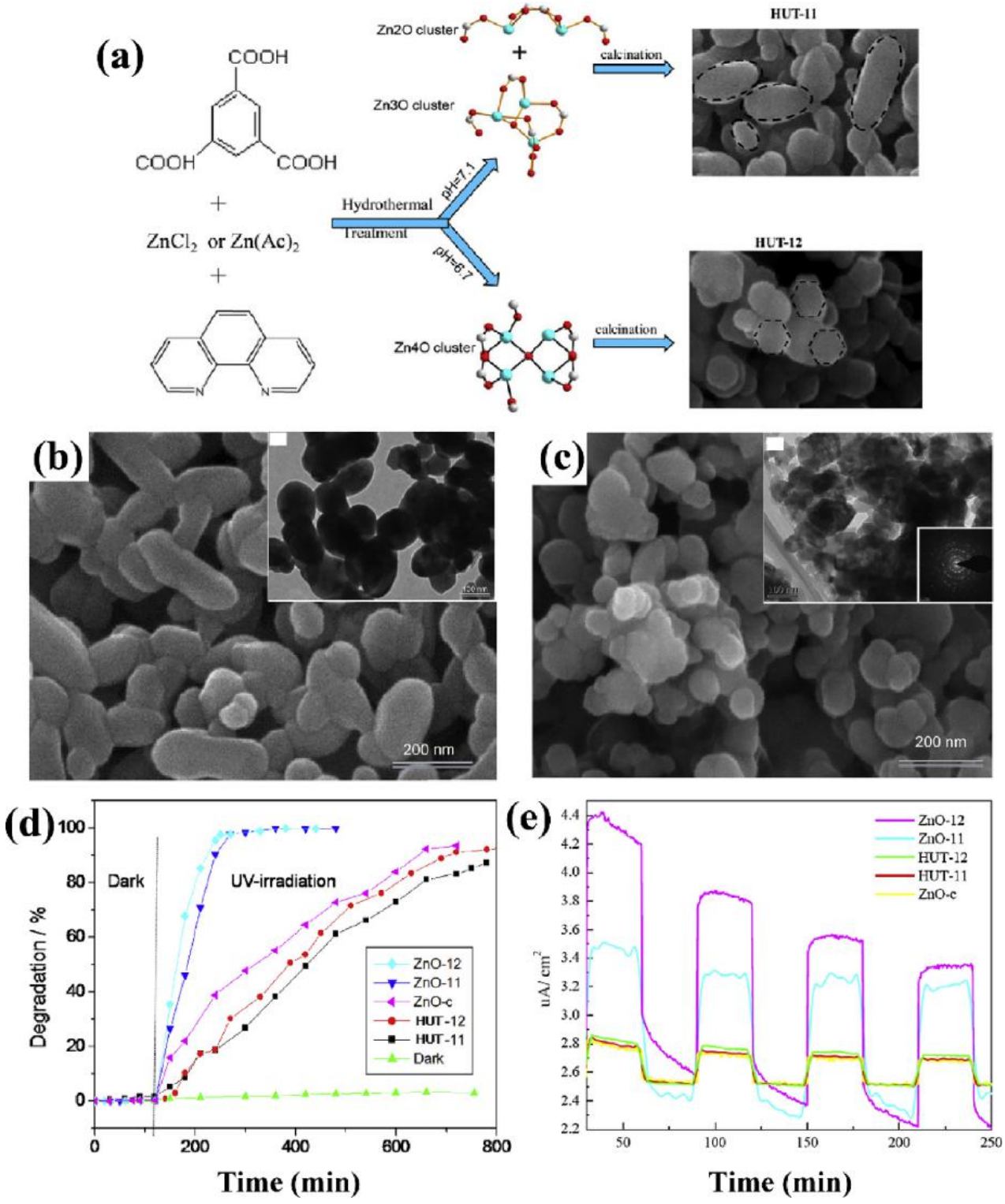

Fig. 10. Synthesis of ZnO nanoparticles from the HUT-11 and HUT-12 (a); SEM images of ZnO-11 (b) and ZnO-12 (c); Performances of Cr(VI) photoreduction over the prepared materials under UV irradiation (d); The transient photocurrent density responses of HUT-11, HUT-12, as well as ZnO-11, ZnO-12 and ZnO-c (e) [82].

environment as well as the metal–oxygen cluster of the two Zn-MOFs. Under the identical conditions, the Cr(VI) reduction rates of ZnO-11 and ZnO-12 were much higher than those of HUT-11, HUT-12, along with commercial ZnO and TiO_2 (P25) nanoparticles. Especially, ZnO-12 derived from HUT-12 with different morphology and particle size from ZnO-11 exhibited higher Cr(VI) removal efficiency (Fig. 10d). Furthermore, ZnO-11 and ZnO-12 showed stronger photocurrent response than those of HUT-11 and HUT-12. In addition, the superior photocurrent density of ZnO-12 to those of commercial ZnO and Zn-MOFs (HUT-11 and HUT-12) indicated that the obtained ZnO nanoparticles were excellent photocatalysts with the advantage of efficient separation of photoinduced carriers (Fig. 10e) [178]. However, the as-prepared ZnO-12 still suffered from poor recyclability and reuse due to the unavoidable photo-corrosion of ZnO under UV irradiation [179], which can be overcome by introducing some other

semiconductors. In all, these two Zn-MOFs afforded unique ZnO with tunable morphologies as well as particle sizes, in which the ZnO nanoparticles with smaller particle size demonstrated superior performances. Therefore, it is practicable to prepare metal oxides semiconductors with adjustable size and properties via calcination.

4. Catalytic reduction

Catalytic hydrogenation is deemed as an effective and cost-competitive technique to eliminate reducible pollutants in water [180]. It has been reported that Cr(VI) can be reduced to Cr(III) by some catalysts with the aid of reducing agents like humic acid or formic acid [27,181,182]. Different from other monocarboxylic acids, formic acid (HCOOH) can be directly mineralized to CO_2 and H_2 ($HCOOH \rightarrow CO_2 + H_2$) in the presence of metal catalysts, thereby acting as a desired sacrificial agent in Cr(VI) reduction [183]. At present, various MOF-derived metal containing catalyst including non-precious (like Ni, Fe) and precious metal catalyst (like Cu, Pd) are explored for catalytic hydrogenation.

4.1. Ni@carbon

Ni nanoparticles (NPs), a non-precious metal catalyst, have arose wide attention because they have the characteristics of high catalytic activity as well as low toxicity and production. However, the low stability and efficiency of Ni NPs become the main challenge in the catalytic process [184]. It has been reported that embedding Ni NPs on a three-dimensional (3D) structure could be an effective way to improve catalytic activity [185]. Lv et al. [84] prepared different Ni@carbon composites by high temperature pyrolysis toward yolk shell-like Ni-MOF. Synthetic process of Ni@carbon was depicted in Fig. 11a. PXRD patterns, TEM images and Raman spectra confirmed formation of Ni@carbon and its yolk shell-like structure (Fig. 11b and 11e). It was speculated that NiO was firstly formed from Ni(II) in MOF and then the metallic Ni was produced by NiO reduction with the increase of calcination temperature. The surface charge of Ni@carbon450 is positive at pH < 4.37 and negative at pH > 4.37. The obtained porous carbon materials have a large specific surface area and a layered structure similar to Ni-MOF, regular porous structure and rich Ni content, which are favorable for its catalytic activity.

In the presence of formic acid, as depicted in Fig. 11c and 11d, Ni@carbon450 with a pyrolysis temperature of 450 ℃ has a higher ability ($k = 1.442\ min^{-1}$) to catalytic Cr(VI) reduction compared to carbon550 ($k = 0.0837\ min^{-1}$), in which the Cr(VI) was completely reduced at 30 min. In addition, the effects of different pH, initial Cr(VI) concentration, temperature and formic acid concentration on Ni@carbon450 catalytic reduction of Cr(VI) indicated that lower pH, higher temperature and formic acid concentration favored improvement of catalytic reduction efficiency. The catalytic Cr(VI) removal rate decreased slightly with the increase of the number of cycles' operation, but the catalytic efficiency still remained at 87% after 10 cycles. The mechanism of catalytic reduction of Cr(VI) can be deduced from Raman spectrum, PXRD, magnetization curve, X-ray photoelectron spectroscopy (XPS) and H_2 production rate. All the characterizations of Ni@carbon450 after catalytic reaction indicated that a small fraction of Ni was oxidized to Ni(II). As shown in Fig. 11f, the Cr(VI) reduction

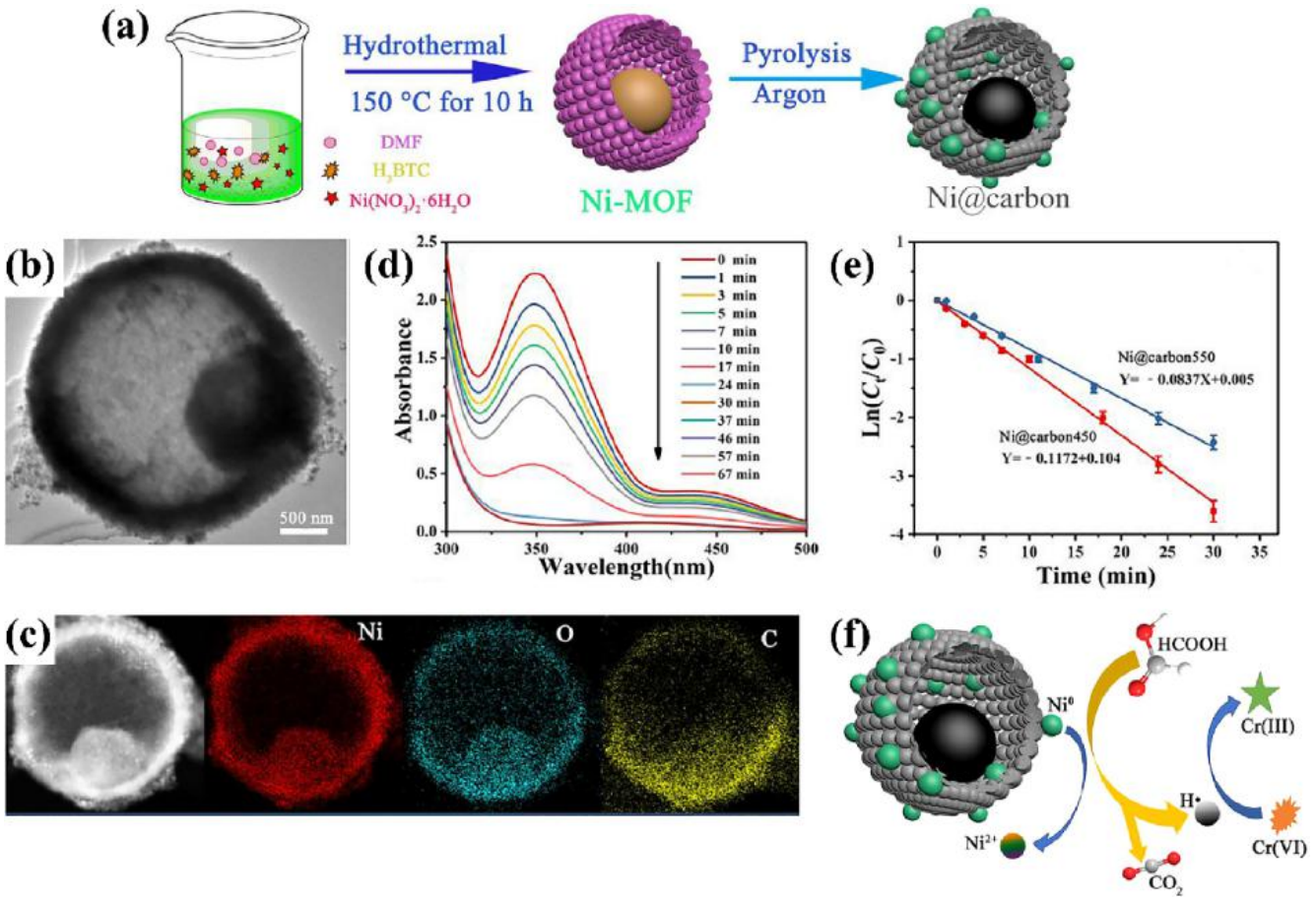

Fig. 11. Synthetic process of Ni@carbon (a); TEM image of Ni@carbon (b); The changes of UV–vis spectra over time during Cr(VI) reduction with the aid of HCOOH by Ni@carbon450 (c); The reduction rate of Cr(VI) by Ni@carbon450 and Ni@carbon550 (d); HAADF-STEM-EDS images (e) of Ni@carbon450; The mechanism of Cr (VI) reduction over Ni@carbon450 with the aid of HCOOH (f) [84].

mechanism could be described that formic acid and Cr(VI) were firstly enriched on the material due to the electrostatic interaction between the surface of the material and formic acid/Cr(VI). The large pores and regular structure made Cr(VI) easily enter the interior of the material, which promoted intimate contact between Cr(VI) and active sites. Formic acid was decomposed into CO_2 and hydrogen (H·) with the existence of Ni through dehydrogenation. The formed H· displayed the capacity of reducing Cr(VI) to Cr(III). The Ni(0) presented in Ni@carbon450 could be oxidized to Ni(II) in the catalytic process. Therefore, the catalytic Cr(VI) reduction of Ni@carbon450 with the aid of electron donor acid was achieved by H· transfer. This work provided a new strategy to fabricate noble catalyst by carbonization of MOFs self-sacrifice template, which could achieve excellent Cr(VI) reduction performances in the presence of electron donor acid.

4.2. PdCu/N-doped carbon/graphene nanosheets

Metal nanoparticles (like ZVI, Pt NPs, Pb NPs, etc.) have attracted wide attention due to their controllable size, fascinating properties and practical application [4,186]. The dispersibility of metal nanoparticles exerts a direct effect on the practical performance, so that suitable substrate should be explored to be a mechanical support of NPs to stabilize them [187]. It has found that metal NPs could be encapsulated or functionalized by MOF-derived materials. In addition, the metal nanoparticles and MOFs derivatives composites can benefit from the porosity of MOFs to prevent the aggregation of metal nanoparticles and improve the performance [188].

Liu and co-workers [86] immobilized PdCu nanoalloys in N-doped carbon/graphene nanosheets (NCG) from graphite oxide (GO)/ZIF-8 precursors to achieve Cr(VI) catalytic reduction. Firstly, NCG was prepared via the carbonization of GO/ZIF-8. The NCG was added into Na_2PdCl_4 and $CuCl_2$ solution to conduct hydrazine-involved hydrothermal reaction to obtain PdCu/NCG. TEM images demonstrated that PdCu alloy NPs were uniformly immersed in NCG nanosheets, indicating that stabilizing PdCu nanoalloys on NCG could lessen the interaction between particles to improve the dispersibility (Fig. 12a and 12c). In the presence of formic acid, PdCu/NCG exhibited higher catalytic rate than PdCu, NCG, Pd/NCG ($0.380\ min^{-1}$) and Cu/NCG ($0.031\ min^{-1}$), which confirmed the enhanced catalytic performances due to introduction of PdCu (Fig. 12b). PdCu/NCG exhibited highest Cr (VI) reduction efficiency at pH = 2.0, and the performance decreased with the increasing pH values. It is worth noting that the catalytic efficiency decreased as pH = 1.0, because the Cr(VI) catalytic reduction is the process of producing active H ($HCOOH \leftrightarrow HCOO_{ads}^{-} + H^{+}$) by formic acid. Excessively low pH values will compel the formate intermediate to return to formic acid, which was not conductive the reduction. Generally speaking, the d-band center (ε_d) represents the affinity of the metal atom to the adsorbate [189]. Density Functional Theory (DFT) calculations demonstrated an increase in ε_d of PdCu nanoalloys which can facilitate strong chemisorption of formic acid compared with single metal Pd or Cu. The adsorbed formic acid will be activated to generate active H atoms on the PdCu alloy, which displayed strong reducing capacity and reduced Cr(VI) to Cr(III) immediately (Fig. 12e). Immobilizing PdCu nanoalloys into NCG induced electronic modification into PdCu/NCG, which accounted for boosted catalytic performances coupled with the porosity of NCG nanosheets. This work afforded a novel insight into the interaction between metal nanoalloys and MOF derivatives composites.

4.3. Ni@ N-doped GO-CNT

Up to now, the development of efficient novel catalysts has attracted wide attention. Among them, it has been reported that transition metals encapsulated in nitrogen-doped carbon materials (TMs@N-C) display particular merits of high catalytic property, avoiding TMs' corrosion as well as adequate active sites [190,191]. TMs@N-C with N-containing MOFs as precursors exhibited series of issues such as low N-doping content, metal NPs aggregation and low surface area. In order to solve the problems, Chen and co-workers [85] prepared a 3D N-doped GO-CNT framework with well-packed nickel nanoparticles (Ni@N-CNTs/N-G) (Fig. 13a, 13b and 13c) by introducing melamine [192]. Specifically, Ni-MOF was firstly combined with melamine and then being pyrolyzed at 600 ℃, and then the obtained Ni-C_3N_4 was further heated at higher temperature to prepare Ni@N-CNTs/N-G. It is worth noting that g-C_3N_4 provided a template and nitrogen source for the formation of GO and a carbon source for the formation of CNT. The successful fabrication of Ni@N-CNTs/N-G was characterized by XRD, SEM, TEM, Raman spectra and XPS analysis.

The performance of Ni@N-CNTs/N-G at different treated temperatures showed that N-CNTs/NG-800 (treated at 800 ℃) exhibited superior Cr(VI) catalytic reduction efficiency with aid of HCOOH. N-CNTs/NG-800 achieved 99.6% Cr(VI) catalytic efficiency within 50 min (Fig. 13d). Considering the abundant N content and porous structure, the maximum adsorption capacity of N-CNTs/NG-800 was reported as $72.325\ mg\ g^{-1}$ (Fig. 13e), which was assigned to the larger specific surface area ($254.62\ m^2\ g^{-1}$) than N-CNTs/NG-700 and N-CNTs/NG-900. Therefore, the reasons for higher catalytic efficiency of N-CNTs/NG-800 could be also attributed to the enrichment of Cr(VI) on the surface of the three-dimensional structure and abundant catalytic active sites that could promote the adsorption and dehydrogenation of formic acid. The experiments of influence factors demonstrated that lower Cr (VI) concentration and pH values, increased catalysts dosage and temperature were benefit for Cr(VI) removal. The anions including SO_4^{2-} and PO_4^{3-} induced minor impact on catalytic efficiency, while Cl^-, HCO_3^-, and NO_3^- exerted obviously influence on the performances because of the monovalent ions and smaller sizes that could compete with Cr(VI) [193].

Recycle experiments revealed that the removal efficiency was still 82.7% after 10 cycles (Fig. 13f), and the cumulative Ni^{2+} concentration was only $95\ \mu g\ L^{-1}$ due to the protection of N-CNT/NG. The amount of Ni^{2+} dissolution was further reduced after several runs, which showed that the 3D Ni@N -CNTs/NG-800 catalyst was stable and reusable. According to XPS analysis and gas volume produced experiments, the catalytic mechanism could be attributed to the catalytic reduction assisted by HCOOH, the nitrogen-triggered reduction and functional groups on the material surface. To be exact, monoatomic hydrogen was produced by HCOOH in the presence of metal Ni, which can immediately achieve Cr(VI) reduction. In addition, Cr(VI) could be reduced to Cr(III) by nitrogen and functional groups inside the material. Therefore, it can be concluded that the main reason for Cr(VI) reduction over the Ni@N-CNTs/N-G in the presence of HCOOH was the generated ·H, while the groups including nitrogen and oxygen groups as well as N-induced reduction played a minor role (Fig. 13g). Encapsulating nickel nanoparticles into N-doped GO-CNT could avoided corrosion and leakage of the metal catalyst. This work provided a method of constructing novel nonnoble metal-based catalyst, which could effectively promote toxic heavy metals catalytic removal.

5. Conclusions and prospects

Considering that MOFs benefit from larger specific surface area, high porosity, as well as flexible structure and function, using MOFs as precursors or sacrificial templates is deemed as one of the effective methods to prepare novel materials with unique structures. MOF-derived materials maintained large specific surface areas, regular structures, and abundant porosity, which enable contaminants easily entering the material to contact with the active sites and promote the charge transfer rate. In addition, the porous metal composites derived from MOFs also provide a capsulation for the metal and prevent the leakage of metal ions and the collapse of the structure, which could be suitable for the practical application. At present, the preparation of MOF derivatives mainly includes solvothermal method and calcination

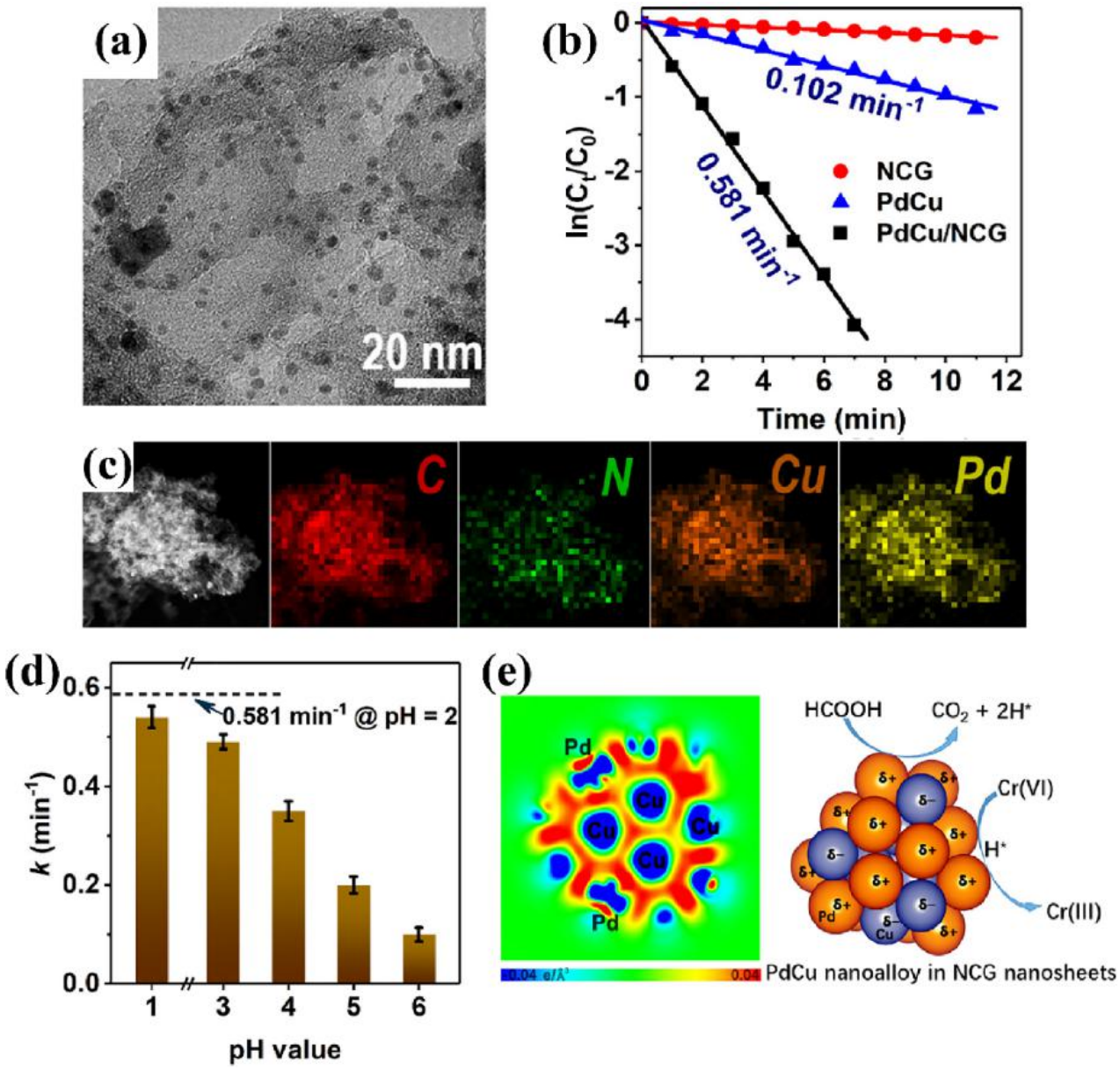

Fig. 12. TEM image of PdCu/NCG (a); Relation of $\ln(C_t/C_0)$ and reaction time for the Cr(VI) reduction over PdCu/NCG, PdCu nanoalloy and NCG (b); HAADF-STEM and the elemental mapping images of PdCu/NCG (c); Histogram of k at different pH values (d); the Cr(VI) removal mechanisms over PdCu/NCG (e) [86].

or pyrolysis method to obtain metal sulfides, oxides and porous carbon materials. These methods are often one-step synthesis and accessible to achieve. In addition, modification of MOFs derivatives is mainly achieved by two methods: (i) MOFs composited with modified materials are treated to prepared derivatives composites [194–198]; (ii) Direct derivatives of MOFs are first prepared, and then combined with specific materials [199–201]. At present, some modification methods for MOFs derivatives like integrating MOFs derivatives with conductors [147], semiconductors [202,203] and polymers [204] have also been investigated.

The Cr(VI) removal with the aid of MOF derivatives and their composites provides various materials and techniques for chrome-containing wastewater treatment. MOF derivatives for Cr(VI) removal are usually through adsorption, catalytic reduction and photocatalytic reduction, and even the combination of adsorption and reduction. The applications of MOF derivatives for the Cr(VI) removal have achieved significant advances, however, there are still emerging issues to be considered: (i) High throughput production of various MOFs with low cost was urgently needed. The practical applications of MOFs are restricted by commercial availability and costs. Up to now, only a small number of MOF products are produced commercially by international companies [48]. As the most popular method for MOFs synthesis, solvent-thermal method (hydrothermal method) can precisely control the particle size, shape and crystallinity of the products. However, the solvothermal synthesis displays many disadvantages of long reaction time (hours or even days), low yield, large consumption of organic solvents and high cost [205]. Therefore, the methods of increasing the mass production of MOF and reducing its cost should be further explored. At present, many attempts have been adopted to improve the yield of MOF, such as electrochemical method and mechanochemical method. However, further exploration should be proceeded. (ii) Preparation methods of MOF derivatives and their composites should be enhanced. The preparation of materials directly derived from MOF via calcination and pyrolysis often requires higher energy. The preparation methods of composite materials of MOF derivatives is often time-consuming and complicated. Therefore, it is necessary to reduce the

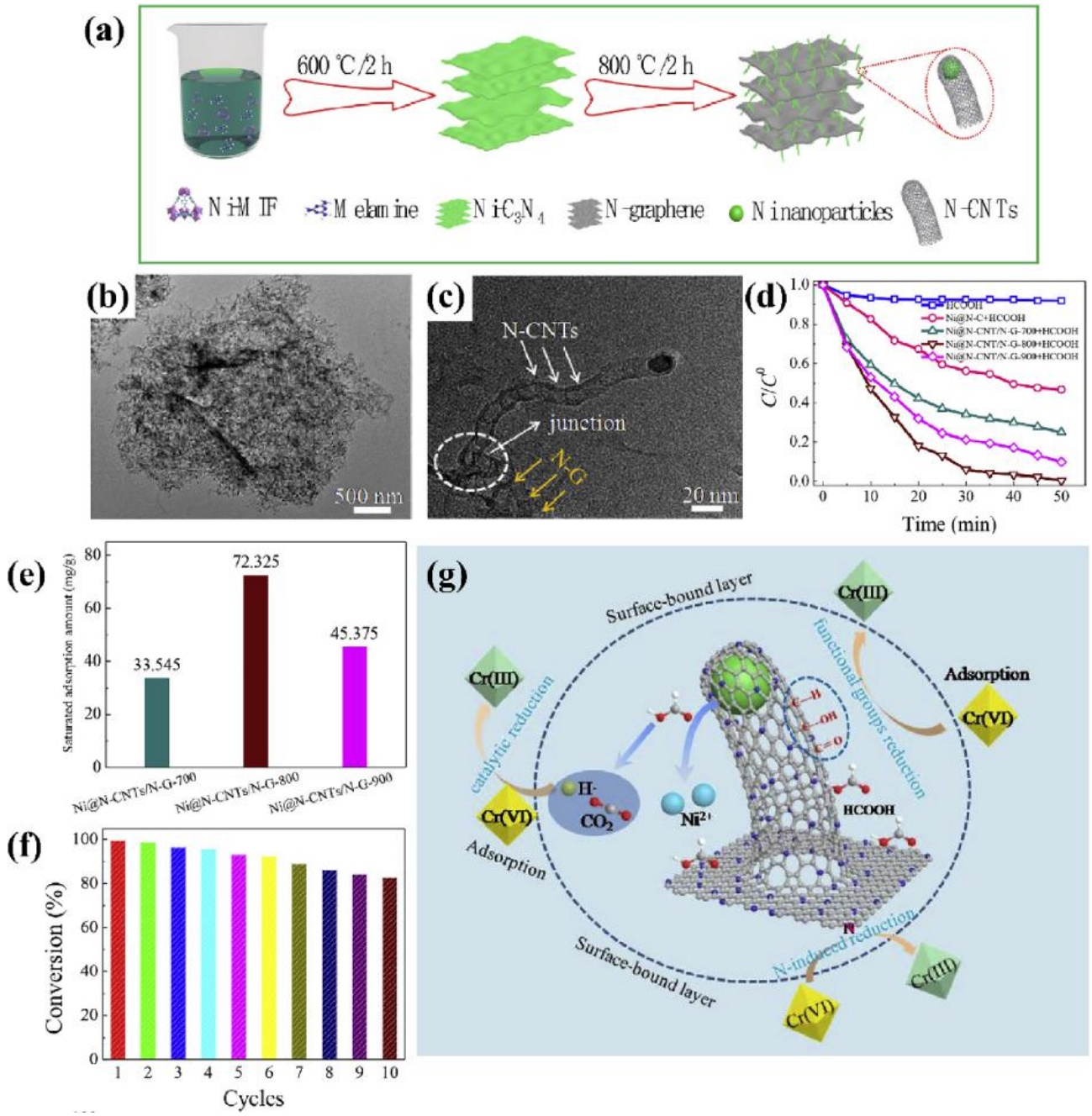

Fig. 13. The synthesis process of Ni@N-CNTs/N-G-x hybrids (a); TEM image of Ni@N-CNTs/N-G-800 (b) and (c); The Cr(VI) reduction in different systems (d); the Cr (VI) adsorption capacity of Ni@N-CNTs/N-G-x (e); Catalytic stability and reusability of 3D Ni@N-CNTs/N-G-800 (f); The proposed mechanism toward Cr(VI) reduction by Ni@N-CNTs/N-G with the aid of HCOOH (g) [85].

production cost of MOF-derived materials and develop green and environmental protection technology. (iii) Cr(VI) removal under different circumstances should be investigated. Cr(VI) concentrations and pH values in surface water and diverse wastewater are various so that the removal efficiencies of MOF derivatives are different. It has been found that Cr(VI) removal efficiency in the catalysis and adsorption processes could be dramatically promoted at low pH values. In addition, MOF derived materials exhibit different performances at varied concentrations with treated methods like adsorption, photocatalysis and catalysis. However, the stability of MOF derivatives under different pH values, impact of excessive acid on environment and subsequent treatment as well as treatment cost should be taken into full consideration. Therefore, it is of great importance to select appropriate MOF derivatives to achieve Cr(VI) removal under different circumstances. (iv) Previous reports have proved that by adding some nontoxic hole trapping agents (small molecule organic acids, etc.), the photocatalytic Cr(VI) reduction efficiency can be greatly improved, in which the reduction and oxidation can also be achieved simultaneously [206–208]. Also, with the coexistence of multiple pollutants, there are also many studies that make full use of the role of photogenerated electrons and holes to achieve the simultaneous reduction of Cr(VI) and oxidation of organic pollutants [167,209]. Simultaneous reduction and oxidation can effectively improve the water treatment efficiency for multicomponent complex wastewater. (v) For photocatalytic Cr(VI) reduction, different light sources will affect the performance of photocatalysis [210]. According to different bandgap and light source conditions, the suitable light source (like visible light, ultraviolet light or solar light) is selected to achieve the balance between photocatalytic

efficiency and cost.

In all, the reported fabrication strategies, Cr(VI) removal performances and proposed mechanisms, along with the current challenges for MOF derivatives have been reviewed and highlighted in this article, which can provide intensive perception in further investigation and utilization of MOF derivatives and their composites for pollutants elimination in environmental remediation with the purpose of sustainable development.

Declaration of Competing Interest

The authors declare that they have no known competing financial interests or personal relationships that could have appeared to influence the work reported in this paper.

Acknowledgements

This work was supported by National Natural Science Foundation of China (51878023), Beijing Natural Science Foundation (8202016), Great Wall Scholars Training Program Project of Beijing Municipality Universities (CIT&TCD20180323), and Beijing Talent Project (2019A22).

References

[1] O. Karnitz, L.V.A. Gurgel, J.C.P. de Melo, V.R. Botaro, T.M.S. Melo, R.P. de Freitas Gil, L.F. Gil, Adsorption of heavy metal ion from aqueous single metal solution by chemically modified sugarcane bagasse, Bioresour. Technol. 98 (2007) 1291–1297.
[2] M.A. Barakat, New trends in removing heavy metals from industrial wastewater, Arabian J. Chem. 4 (2011) 361–377.
[3] C. Raji, T.S. Anirudhan, Batch Cr(VI) removal by polyacrylamide-grafted sawdust: Kinetics and thermodynamics, Water Res. 32 (1998) 3772–3780.
[4] C.-C. Wang, X.-D. Du, J. Li, X.-X. Guo, P. Wang, J. Zhang, Photocatalytic Cr(VI) reduction in metal-organic frameworks: A mini-review, Appl. Catal. B 193 (2016) 198–216.
[5] Y. Liu, F. Liu, N. Ding, X. Hu, C. Shen, F. Li, M. Huang, Z. Wang, W. Sand, C.-C. Wang, Recent advances on electroactive CNT-based membranes for environmental applications: The perfect match of electrochemistry and membrane separation, Chin. Chem. Lett. (2020).
[6] C.E. Barrera-Díaz, V. Lugo-Lugo, B. Bilyeu, A review of chemical, electrochemical and biological methods for aqueous Cr(VI) reduction, J. Hazard. Mater. 223–224 (2012) 1–12.
[7] M. Costa, Toxicity and carcinogenicity of Cr (VI) in animal models and humans, Crit. Rev. Toxicol. 27 (1997) 431–442.
[8] M. Bhaumik, A. Maity, V. Srinivasu, M.S. Onyango, Enhanced removal of Cr (VI) from aqueous solution using polypyrrole/Fe_3O_4 magnetic nanocomposite, J. Hazard. Mater. 190 (2011) 381–390.
[9] E. Demirbas, M. Kobya, E. Senturk, T. Ozkan, Adsorption kinetics for the removal of chromium (VI) from aqueous solutions on the activated carbons prepared from agricultural wastes, Water Sa 30 (2004) 533–539.
[10] Y.-X. Li, X. Wang, C.-C. Wang, H. Fu, Y. Liu, P. Wang, C. Zhao, S-TiO_2/UiO-66-NH_2 composite for boosted photocatalytic Cr(VI) reduction and bisphenol A degradation under LED visible light, J. Hazard. Mater. 399 (2020) 123085.
[11] H. Jabeen, V. Chandra, S. Jung, J.W. Lee, K.S. Kim, S.B. Kim, Enhanced Cr(vi) removal using iron nanoparticle decorated graphene, Nanoscale 3 (2011) 3583–3585.
[12] I. Narin, A. Kars, M. Soylak, A novel solid phase extraction procedure on Amberlite XAD-1180 for speciation of Cr(III), Cr(VI) and total chromium in environmental and pharmaceutical samples, J. Hazard. Mater. 150 (2008) 453–458.
[13] N.R. Bishnoi, M. Bajaj, N. Sharma, A. Gupta, Adsorption of Cr(VI) on activated rice husk carbon and activated alumina, Bioresour. Technol. 91 (2004) 305–307.
[14] W. Jiang, M. Pelaez, D.D. Dionysiou, M.H. Entezari, D. Tsoutsou, K. O'Shea, Chromium(VI) removal by maghemite nanoparticles, Chem. Eng. J. 222 (2013) 527–533.
[15] X.-D. Du, X.-H. Yi, P. Wang, W. Zheng, J. Deng, C.-C. Wang, Robust photocatalytic reduction of Cr(VI) on UiO-66-NH_2(Zr/Hf) metal-organic framework membrane under sunlight irradiation, Chem. Eng. J. 356 (2019) 393–399.
[16] F.-X. Wang, X.-H. Yi, C.-C. Wang, J.-G. Deng, Photocatalytic Cr(VI) reduction and organic-pollutant degradation in a stable 2D coordination polymer, Chin. J. Catal. 38 (2017) 2141–2149.
[17] C. Peng, H. Meng, S. Song, S. Lu, A. Lopez-Valdivieso, Elimination of Cr (VI) from electroplating wastewater by electrodialysis following chemical precipitation, Sep. Sci. Technol. 39 (2005) 1501–1517.
[18] C.E. Barrera-Díaz, V. Lugo-Lugo, B. Bilyeu, A review of chemical, electrochemical and biological methods for aqueous Cr (VI) reduction, J. Hazard. Mater. 223 (2012) 1–12.
[19] S. Jamshidifard, S. Koushkbaghi, S. Hosseini, S. Rezaei, A. Karamipour, M. Irani, Incorporation of UiO-66-NH_2 MOF into the PAN/chitosan nanofibers for adsorption and membrane filtration of Pb (II), Cd (II) and Cr (VI) ions from aqueous solutions, J. Hazard. Mater. 368 (2019) 10–20.
[20] J. Sánchez, B.L. Rivas, Cationic hydrophilic polymers coupled to ultrafiltration membranes to remove chromium (VI) from aqueous solution, Desalination 279 (2011) 338–343.
[21] Q. Ge, X. Feng, R. Wang, R. Zheng, S. Luo, L. Duan, Y. Ji, J. Lin, H. Chen, Mixed Redox-couple Involved Chalcopyrite Phase $CuFeS_2$ Quantum Dots for Highly Efficient Cr(VI) Removal, Environ. Sci. Technol. 54 (2020) 8022–8031.
[22] T. Karthikeyan, S. Rajgopal, L.R. Miranda, Chromium(VI) adsorption from aqueous solution by Hevea Brasilinesis sawdust activated carbon, J. Hazard. Mater. 124 (2005) 192–199.
[23] F. Wu, T. Zhao, Y. Yao, T. Jiang, B. Wang, M. Wang, Recycling supercapacitor activated carbons for adsorption of silver (I) and chromium (VI) ions from aqueous solutions, Chemosphere 238 (2020) 124638.
[24] A.C. Zimmermann, A. Mecabô, T. Fagundes, C.A. Rodrigues, Adsorption of Cr(VI) using Fe-crosslinked chitosan complex (Ch-Fe), J. Hazard. Mater. 179 (2010) 192–196.
[25] F.-Q. Shao, J.-J. Feng, X.-X. Lin, L.-Y. Jiang, A.-J. Wang, Simple fabrication of AuPd@Pd core-shell nanocrystals for effective catalytic reduction of hexavalent chromium, Appl. Catal. B 208 (2017) 128–134.
[26] M.J. Alowitz, M.M. Scherer, Kinetics of Nitrate, Nitrite, and Cr(VI) Reduction by Iron Metal, Environ. Sci. Technol. 36 (2002) 299–306.
[27] M.A. Omole, I.O. K'Owino, O.A. Sadik, Palladium nanoparticles for catalytic reduction of Cr(VI) using formic acid, Appl. Catal. B 76 (2007) 158–167.
[28] Y. Li, W. Cui, L. Liu, R. Zong, W. Yao, Y. Liang, Y. Zhu, Removal of Cr(VI) by 3D TiO_2-graphene hydrogel via adsorption enriched with photocatalytic reduction, Appl. Catal. B 199 (2016) 412–423.
[29] L.B. Khalil, W.E. Mourad, M.W. Rophael, Photocatalytic reduction of environmental pollutant Cr(VI) over some semiconductors under UV/visible light illumination, Appl. Catal. B 17 (1998) 267–273.
[30] X. Wang, Y.-X. Li, X.-H. Yi, C. Zhao, P. Wang, J. Deng, C.-C. Wang, Photocatalytic Cr(VI) elimination over BUC-21/N-$K_2Ti_4O_9$ composites: Big differences in performance resulting from small differences in composition, Chin. J. Catal. 42 (2021) 259–270.
[31] C.J. Doonan, C.J. Sumby, Metal–organic framework catalysis, CrystEngComm 19 (2017) 4044–4048.
[32] Y.-B. Huang, J. Liang, X.-S. Wang, R. Cao, Multifunctional metal–organic framework catalysts: synergistic catalysis and tandem reactions, Chem. Soc. Rev. 46 (2017) 126–157.
[33] S.-H. Huo, X.-P. Yan, Metal–organic framework MIL-100 (Fe) for the adsorption of malachite green from aqueous solution, J. Mater. Chem. 22 (2012) 7449–7455.
[34] F.-J. Ma, S.-X. Liu, C.-Y. Sun, D.-D. Liang, G.-J. Ren, F. Wei, Y.-G. Chen, Z.-M. Su, A sodalite-type porous metal − organic framework with polyoxometalate templates: adsorption and decomposition of dimethyl methylphosphonate, J. Am. Chem. Soc. 133 (2011) 4178–4181.
[35] T. Song, L. Zhang, P. Zhang, J. Zeng, T. Wang, A. Ali, H. Zeng, Stable and improved visible-light photocatalytic hydrogen evolution using copper(ii)–organic frameworks: engineering the crystal structures, J. Mater. Chem. A 5 (2017) 6013–6018.
[36] T. Rodenas, I. Luz, G. Prieto, B. Seoane, H. Miro, A. Corma, F. Kapteijn, F.X.L. i Xamena, J. Gascon, Metal–organic framework nanosheets in polymer composite materials for gas separation, Nat. Mater. 14 (2015) 48–55.
[37] Z.R. Herm, B.M. Wiers, J.A. Mason, J.M. van Baten, M.R. Hudson, P. Zajdel, C.M. Brown, N. Masciocchi, R. Krishna, J.R. Long, Separation of hexane isomers in a metal-organic framework with triangular channels, Science 340 (2013) 960–964.
[38] A. Nuhnen, D. Dietrich, S. Millan, C. Janiak, Role of filler porosity and filler/polymer interface volume in metal–organic framework/polymer mixed-matrix membranes for gas separation, ACS Appl. Mater. Interfaces 10 (2018) 33589–33600.
[39] M.C. So, G.P. Wiederrecht, J.E. Mondloch, J.T. Hupp, O.K. Farha, Metal–organic framework materials for light-harvesting and energy transfer, Chem. Commun. 51 (2015) 3501–3510.
[40] A. Cadiau, Y. Belmabkhout, K. Adil, P.M. Bhatt, R.S. Pillai, A. Shkurenko, C. Martineau-Corcos, G. Maurin, M. Eddaoudi, Hydrolytically stable fluorinated metal-organic frameworks for energy-efficient dehydration, Science 356 (2017) 731–735.
[41] M. Bagheri, M.Y. Masoomi, A. Morsali, A. Schoedel, Two dimensional host–guest metal–organic framework sensor with high selectivity and sensitivity to picric acid, ACS Appl. Mater. Interfaces 8 (2016) 21472–21479.
[42] B. Gole, A.K. Bar, P.S. Mukherjee, Fluorescent metal–organic framework for selective sensing of nitroaromatic explosives, Chem. Commun. 47 (2011) 12137–12139.
[43] C.-C. Wang, X. Wang, W. Liu, The synthesis strategies and photocatalytic performances of TiO_2/MOFs composites: A state-of-the-art review, Chem. Eng. J. 391 (2020) 123601.
[44] M. Li, Y. Liu, C. Shen, F. Li, C.-C. Wang, M. Huang, B. Yang, Z. Wang, J. Yang, W. Sand, One-step Sb(III) decontamination using a bifunctional photoelectrochemical filter, J. Hazard. Mater. 389 (2020) 121840.
[45] Q.-L. Zhu, Q. Xu, Metal–organic framework composites, Chem. Soc. Rev. 43 (2014) 5468–5512.
[46] H. Li, M. Eddaoudi, M. O'Keeffe, O.M. Yaghi, Design and synthesis of an exceptionally stable and highly porous metal-organic framework, Nature 402 (1999) 276–279.
[47] Y.-R. Lee, J. Kim, W.-S. Ahn, Synthesis of metal-organic frameworks: A mini

review, Korean J. Chem. Eng. 30 (2013) 1667–1680.
[48] J. Ren, X. Dyosiba, N.M. Musyoka, H.W. Langmi, M. Mathe, S. Liao, Review on the current practices and efforts towards pilot-scale production of metal-organic frameworks (MOFs), Coord. Chem. Rev. 352 (2017) 187–219.
[49] M. Rubio-Martinez, C. Avci-Camur, A.W. Thornton, I. Imaz, D. Maspoch, M.R. Hill, New synthetic routes towards MOF production at scale, Chem. Soc. Rev. 46 (2017) 3453–3480.
[50] M. Klimakow, P. Klobes, A.F. Thünemann, K. Rademann, F. Emmerling, Mechanochemical Synthesis of Metal−Organic Frameworks: A Fast and Facile Approach toward Quantitative Yields and High Specific Surface Areas, Chem. Mater. 22 (2010) 5216–5221.
[51] J. Klinowski, F.A. Almeida Paz, P. Silva, J. Rocha, Microwave-Assisted Synthesis of Metal-Organic Frameworks, Dalton Trans. 40 (2011) 321–330.
[52] W.-J. Son, J. Kim, J. Kim, W.-S. Ahn, Sonochemical synthesis of MOF-5, Chem. Commun. (2008) 6336–6338.
[53] R. Ameloot, L. Stappers, J. Fransaer, L. Alaerts, B.F. Sels, D.E. De Vos, Patterned Growth of Metal-Organic Framework Coatings by Electrochemical Synthesis, Chem. Mater. 21 (2009) 2580–2582.
[54] B. Ni, C. Ouyang, X. Xu, J. Zhuang, X. Wang, Modifying commercial carbon with trace amounts of ZIF to prepare derivatives with superior ORR activities, Adv. Mater. 29 (2017) 1701354.
[55] H. Tang, M. Zheng, Q. Hu, Y. Chi, B. Xu, S. Zhang, H. Xue, H. Pang, Derivatives of coordination compounds for rechargeable batteries, J. Mater. Chem. A 6 (2018) 13999–14024.
[56] W. Chaikittisilp, K. Ariga, Y. Yamauchi, A new family of carbon materials: synthesis of MOF-derived nanoporous carbons and their promising applications, J. Mater. Chem. A 1 (2013) 14–19.
[57] K.-Y. Zou, Z.-X. Li, Controllable Syntheses of MOF-Derived Materials, Chem. Eur. J. 24 (2018) 6506–6518.
[58] W. Yang, X. Li, Y. Li, R. Zhu, H. Pang, Applications of metal–organic-framework-derived carbon materials, Adv. Mater. 31 (2019) 1804740.
[59] K. Shen, X. Chen, J. Chen, Y. Li, Development of MOF-derived carbon-based nanomaterials for efficient catalysis, ACS Catal. 6 (2016) 5887–5903.
[60] Y.-Z. Chen, R. Zhang, L. Jiao, H.-L. Jiang, Metal–organic framework-derived porous materials for catalysis, Coord. Chem. Rev. 362 (2018) 1–23.
[61] J.-B. Raoof, S.R. Hosseini, R. Ojani, S. Mandegarzad, MOF-derived Cu/nanoporous carbon composite and its application for electro-catalysis of hydrogen evolution reaction, Energy 90 (2015) 1075–1081.
[62] S.J. Yang, T. Kim, J.H. Im, Y.S. Kim, K. Lee, H. Jung, C.R. Park, MOF-derived hierarchically porous carbon with exceptional porosity and hydrogen storage capacity, Chem. Mater. 24 (2012) 464–470.
[63] W. Xia, A. Mahmood, R. Zou, Q. Xu, Metal–organic frameworks and their derived nanostructures for electrochemical energy storage and conversion, Energy Environ. Sci. 8 (2015) 1837–1866.
[64] S.J. Yang, J.H. Im, T. Kim, K. Lee, C.R. Park, MOF-derived ZnO and ZnO@ C composites with high photocatalytic activity and adsorption capacity, J. Hazard. Mater. 186 (2011) 376–382.
[65] N. Bakhtiari, S. Azizian, S.M. Alshehri, N.L. Torad, V. Malgras, Y. Yamauchi, Study on adsorption of copper ion from aqueous solution by MOF-derived nanoporous carbon, Microporous Mesoporous Mater. 217 (2015) 173–177.
[66] D. Chen, C. Chen, W. Shen, H. Quan, S. Chen, S. Xie, X. Luo, L. Guo, MOF-derived magnetic porous carbon-based sorbent: synthesis, characterization, and adsorption behavior of organic micropollutants, Adv. Powder Technol. 28 (2017) 1769–1779.
[67] X. Cao, C. Tan, M. Sindoro, H. Zhang, Hybrid micro-/nano-structures derived from metal–organic frameworks: preparation and applications in energy storage and conversion, Chem. Soc. Rev. 46 (2017) 2660–2677.
[68] M. Aleksandrzak, D. Baranowska, T. Kedzierski, K. Sielicki, S. Zhang, M. Biegun, E. Mijowska, Superior synergy of g-C_3N_4/Cd compounds and Al-MOF-derived nanoporous carbon for photocatalytic hydrogen evolution, Appl. Catal. B 257 (2019) 117906.
[69] D.P. Kumar, J. Choi, S. Hong, D.A. Reddy, S. Lee, T.K. Kim, Rational synthesis of metal–organic framework-derived noble metal-free nickel phosphide nanoparticles as a highly efficient cocatalyst for photocatalytic hydrogen evolution, ACS Sustainable Chem. Eng. 4 (2016) 7158–7166.
[70] M.H. Yap, K.L. Fow, G.Z. Chen, Synthesis and applications of MOF-derived porous nanostructures, Green Energy Environ. 2 (2017) 218–245.
[71] S. Xu, Y. Lv, X. Zeng, D. Cao, ZIF-derived nitrogen-doped porous carbons as highly efficient adsorbents for removal of organic compounds from wastewater, Chem. Eng. J. 323 (2017) 502–511.
[72] X. Cui, W. Zuo, M. Tian, Z. Dong, J. Ma, Highly efficient and recyclable Ni MOF-derived N-doped magnetic mesoporous carbon-supported palladium catalysts for the hydrodechlorination of chlorophenols, J. Mol. Catal. A: Chem. 423 (2016) 386–392.
[73] D. Chen, W. Shen, S. Wu, C. Chen, X. Luo, L. Guo, Ion exchange induced removal of Pb (II) by MOF-derived magnetic inorganic sorbents, Nanoscale 8 (2016) 7172–7179.
[74] X. Li, Y. Liu, C. Zhang, T. Wen, L. Zhuang, X. Wang, G. Song, D. Chen, Y. Ai, T. Hayat, Porous Fe_2O_3 microcubes derived from metal organic frameworks for efficient elimination of organic pollutants and heavy metal ions, Chem. Eng. J. 336 (2018) 241–252.
[75] H. Hu, J. Liu, Z. Xu, L. Zhang, B. Cheng, W. Ho, Hierarchical porous Ni/Co-LDH hollow dodecahedron with excellent adsorption property for Congo red and Cr (VI) ions, Appl. Surf. Sci. 478 (2019) 981–990.
[76] Y. Lai, F. Wang, Y. Zhang, P. Ou, P. Wu, Q. Fang, Z. Chen, S. Li, UiO-66 derived N-doped carbon nanoparticles coated by PANI for simultaneous adsorption and reduction of hexavalent chromium from waste water, Chem. Eng. J. 378 (2019) 122069.
[77] D.T.C. Nguyen, H.T.N. Le, T. Van Tran, O.T.K. Nguyen, T.D. Nguyen, D.-V.N. Vo, T.D. Lam, L.G. Bach, D. Van Thuan, A Simple Route for the Synthesis of Fe/C composite derived from the metal-organic framework MIL-53 (Fe), Mater. Today:. Proc. 18 (2019) 2422–2429.
[78] G. Gao, L. Nie, S. Yang, P. Jin, R. Chen, D. Ding, X.C. Wang, W. Wang, K. Wu, Q. Zhang, Well-defined strategy for development of adsorbent using metal organic frameworks (MOF) template for high performance removal of hexavalent chromium, Appl. Surf. Sci. 457 (2018) 1208–1217.
[79] Y. Fang, J. Wen, H. Zhang, Q. Wang, X. Hu, Enhancing Cr (VI) reduction and immobilization by magnetic core-shell structured NZVI@ MOF derivative hybrids, Environ. Pollut. 260 (2020) 114021.
[80] Y.-X. Li, H. Fu, P. Wang, C. Zhao, W. Liu, C.-C. Wang, Porous tube-like ZnS derived from rod-like ZIF-L for photocatalytic Cr (VI) reduction and organic pollutants degradation, Environ. Pollut. 256 (2020) 113417.
[81] H. Fu, L. Wu, J. Hang, P. Wang, C. Zhao, C.-C. Wang, Room-temperature preparation of MIL-68 and its derivative In_2S_3 for enhanced photocatalytic Cr(VI) reduction and organic pollutant degradation under visible light, J. Alloy. Compd. 837 (2020) 155567.
[82] Q.-Q. Xu, S.-W. Qiu, X.-Y. Xing, Z.-H. Wang, Y.-T. Li, Z.-B. He, T.-Z. Ren, Tuning the morphology of ZnO nanoparticles by Zn-clusters and application on the photoreduction of Cr (VI), Solid State Sci. 58 (2016) 22–29.
[83] Z. Hasan, J. Cho, J. Rinklebe, Y.S. Ok, D.-W. Cho, H. Song, Metal organic framework derived Cu–carbon composite: An efficient non-noble metal catalyst for reduction of hexavalent chromium and pendimethalin, J. Ind. Eng. Chem. 52 (2017) 331–337.
[84] Z. Lv, X. Tan, C. Wang, A. Alsaedi, T. Hayat, C. Chen, Metal-organic frameworks-derived 3D yolk shell-like structure Ni@ carbon as a recyclable catalyst for Cr (VI) reduction, Chem. Eng. J. 123428 (2019).
[85] K. Zhu, C. Chen, S. Lu, X. Zhang, A. Alsaedi, T. Hayat, MOFs-induced encapsulation of ultrafine Ni nanoparticles into 3D N-doped graphene-CNT frameworks as a recyclable catalyst for Cr (VI) reduction with formic acid, Carbon 148 (2019) 52–63.
[86] Q. Zhao, L. Liu, R. Liu, L. Zhu, PdCu nanoalloy immobilized in ZIF-derived N-doped carbon/graphene nanosheets: Alloying effect on catalysis, Chem. Eng. J. 353 (2018) 311–318.
[87] H. Demiral, İ. Demiral, F. Tümsek, B. Karabacakoğlu, Adsorption of chromium(VI) from aqueous solution by activated carbon derived from olive bagasse and applicability of different adsorption models, Chem. Eng. J. 144 (2008) 188–196.
[88] P. Miretzky, A.F. Cirelli, Cr(VI) and Cr(III) removal from aqueous solution by raw and modified lignocellulosic materials: A review, J. Hazard. Mater. 180 (2010) 1–19.
[89] C. Rosales-Landeros, C.E. Barrera-Díaz, B. Bilyeu, V.V. Guerrero, F. Ure, A review on Cr (VI) adsorption using inorganic materials, Am. J. Analyt. Chem. 4 (2013) 8–16.
[90] S. Debnath, U.C. Ghosh, Kinetics, isotherm and thermodynamics for Cr(III) and Cr (VI) adsorption from aqueous solutions by crystalline hydrous titanium oxide, J. Chem. Thermodyn. 40 (2008) 67–77.
[91] Y. Li, J. Wang, Z. Li, Q. Liu, J. Liu, L. Liu, X. Zhang, J. Yu, Ultrasound assisted synthesis of Ca–Al hydrotalcite for U (VI) and Cr (VI) adsorption, Chem. Eng. J. 218 (2013) 295–302.
[92] M. Chirita, I. Grozescu, Fe_2O_3–nanoparticles, physical properties and their photochemical and photoelectrochemical applications, Chem. Bull. 54 (2009) 1–8.
[93] M.A. Batista, A. da Costa, J.M. Bigham, H.d. Santana, D.A. Zaia, J. de Souza, G. Ivan, Mineralogical, Chemical, and Physical Characterization of Synthetic Al-substituted Maghemites ($\square$-$Fe_{2-x}Al_xO_3$), Clays Clay Miner. 58 (2010) 451–461.
[94] S. Zeng, K. Tang, T. Li, Controlled synthesis of α-Fe_2O_3 nanorods and its size-dependent optical absorption, electrochemical, and magnetic properties, J. Colloid Interface Sci. 312 (2007) 513–521.
[95] G. Wu, Y. Cheng, Y. Ren, Y. Wang, Z. Wang, H. Wu, Synthesis and characterization of γ-Fe_2O_3@ C nanorod-carbon sphere composite and its application as microwave absorbing material, J. Alloy. Compd. 652 (2015) 346–350.
[96] Q. Han, Z. Liu, Y. Xu, Z. Chen, T. Wang, H. Zhang, Growth and properties of single-crystalline γ-Fe_2O_3 nanowires, The Journal of Physical Chemistry C 111 (2007) 5034–5038.
[97] N. Jordan, A. Ritter, A.C. Scheinost, S. Weiss, D. Schild, R. Hübner, Selenium(IV) Uptake by Maghemite (γ-Fe_2O_3), Environ. Sci. Technol. 48 (2014) 1665–1674.
[98] A. Uheida, G. Salazar-Alvarez, E. Björkman, Z. Yu, M. Muhammed, Fe_3O_4 and γ-Fe_2O_3 nanoparticles for the adsorption of Co^{2+} from aqueous solution, J. Colloid Interface Sci. 298 (2006) 501–507.
[99] X. Sun, L. Yang, Q. Li, J. Zhao, X. Li, X. Wang, H. Liu, Amino-functionalized magnetic cellulose nanocomposite as adsorbent for removal of Cr(VI): Synthesis and adsorption studies, Chem. Eng. J. 241 (2014) 175–183.
[100] Z. Yang, J. Li, F. Cheng, Z. Chen, X. Dong, BiOBr/protonated graphitic C_3N_4 heterojunctions: intimate interfaces by electrostatic interaction and enhanced photocatalytic activity, J. Alloy. Compd. 634 (2015) 215–222.
[101] T.V. Gerasimova, O.L. Evdokimova, A.S. Kraev, V.K. Ivanov, A.V. Agafonov, Micro-mesoporous anatase TiO_2 nanorods with high specific surface area possessing enhanced adsorption ability and photocatalytic activity, Microporous Mesoporous Mater. 235 (2016) 185–194.
[102] C.-Y. Cao, J. Qu, W.-S. Yan, J.-F. Zhu, Z.-Y. Wu, W.-G. Song, Low-Cost Synthesis of Flowerlike α-Fe_2O_3 Nanostructures for Heavy Metal Ion Removal: Adsorption Property and Mechanism, Langmuir 28 (2012) 4573–4579.
[103] J.-S. Hu, L.-S. Zhong, W.-G. Song, L.-J. Wan, Synthesis of Hierarchically Structured Metal Oxides and their Application in Heavy Metal Ion Removal, Adv. Mater. 20 (2008) 2977–2982.

[104] M. Hua, S. Zhang, B. Pan, W. Zhang, L. Lv, Q. Zhang, Heavy metal removal from water/wastewater by nanosized metal oxides: A review, J. Hazard. Mater. 211–212 (2012) 317–331.

[105] M. Komárek, C.M. Koretsky, K.J. Stephen, D.S. Alessi, V. Chrastný, Competitive Adsorption of Cd(II), Cr(VI), and Pb(II) onto Nanomaghemite: A Spectroscopic and Modeling Approach, Environ. Sci. Technol. 49 (2015) 12851–12859.

[106] L. Deng, H. Zeng, Z. Shi, W. Zhang, J. Luo, Sodium dodecyl sulfate intercalated and acrylamide anchored layered double hydroxides: A multifunctional adsorbent for highly efficient removal of Congo red, J. Colloid Interface Sci. 521 (2018) 172–182.

[107] D. Kang, X. Yu, S. Tong, M. Ge, J. Zuo, C. Cao, W. Song, Performance and mechanism of Mg/Fe layered double hydroxides for fluoride and arsenate removal from aqueous solution, Chem. Eng. J. 228 (2013) 731–740.

[108] X.-Y. Yu, T. Luo, Y. Jia, R.-X. Xu, C. Gao, Y.-X. Zhang, J.-H. Liu, X.-J. Huang, Three-dimensional hierarchical flower-like Mg–Al-layered double hydroxides: highly efficient adsorbents for As(v) and Cr(vi) removal, Nanoscale 4 (2012) 3466–3474.

[109] G. Yilmaz, K.M. Yam, C. Zhang, H.J. Fan, G.W. Ho, In situ transformation of MOFs into layered double hydroxide embedded metal sulfides for improved electrocatalytic and supercapacitive performance, Adv. Mater. 29 (2017) 1606814.

[110] S.T. Farrell, C.B. Breslin, Reduction of Cr(VI) at a Polyaniline Film: Influence of Film Thickness and Oxidation State, Environ. Sci. Technol. 38 (2004) 4671–4676.

[111] A. Olad, R. Nabavi, Application of polyaniline for the reduction of toxic Cr(VI) in water, J. Hazard. Mater. 147 (2007) 845–851.

[112] M.J. Katz, Z.J. Brown, Y.J. Colón, P.W. Siu, K.A. Scheidt, R.Q. Snurr, J.T. Hupp, O.K. Farha, A facile synthesis of UiO-66, UiO-67 and their derivatives, Chem. Commun. 49 (2013) 9449–9451.

[113] P.M. Schoenecker, G.A. Belancik, B.E. Grabicka, K.S. Walton, Kinetics study and crystallization process design for scale-up of UiO-66-NH_2 synthesis, AIChE J. 59 (2013) 1255–1262.

[114] J. Yang, F. Zhang, X. Wang, D. He, G. Wu, Q. Yang, X. Hong, Y. Wu, Y. Li, Porous molybdenum phosphide nano-octahedrons derived from confined phosphorization in UIO-66 for efficient hydrogen evolution, Angew. Chem. Int. Ed. 55 (2016) 12854–12858.

[115] W. Cao, W. Luo, H. Ge, Y. Su, A. Wang, T. Zhang, UiO-66 derived Ru/ZrO_2@C as a highly stable catalyst for hydrogenation of levulinic acid to γ-valerolactone, Green Chem. 19 (2017) 2201–2211.

[116] M. Minella, S. Bertinetti, K. Hanna, C. Minero, D. Vione, Degradation of ibuprofen and phenol with a Fenton-like process triggered by zero-valent iron (ZVI-Fenton), Environ. Res. 179 (2019) 108750.

[117] H.K. Boparai, M. Joseph, D.M. O'Carroll, Kinetics and thermodynamics of cadmium ion removal by adsorption onto nano zerovalent iron particles, J. Hazard. Mater. 186 (2011) 458–465.

[118] S. Guo, H. Wang, W. Yang, H. Fida, L. You, K. Zhou, Scalable synthesis of Ca-doped α-Fe_2O_3 with abundant oxygen vacancies for enhanced degradation of organic pollutants through peroxymonosulfate activation, Appl. Catal. B 262 (2020) 118250.

[119] S. Liang, Z. Jia, W. Zhang, X. Li, W. Wang, H. Lin, L. Zhang, Ultrafast activation efficiency of three peroxides by $Fe_{78}Si_9B_{13}$ metallic glass under photo-enhanced catalytic oxidation: a comparative study, Appl. Catal. B 221 (2018) 108–118.

[120] J.C. Seaman, P.M. Bertsch, L. Schwallie, In Situ Cr(VI) Reduction within Coarse-Textured, Oxide-Coated Soil and Aquifer Systems Using Fe(II) Solutions, Environ. Sci. Technol. 33 (1999) 938–944.

[121] F. dos Santos Coelho, J.D. Ardisson, F.C.C. Moura, R.M. Lago, E. Murad, J.D. Fabris, Potential application of highly reactive Fe(0)/Fe_3O_4 composites for the reduction of Cr(VI) environmental contaminants, Chemosphere 71 (2008) 90–96.

[122] Y. Wu, J. Zhang, Y. Tong, X. Xu, Chromium (VI) reduction in aqueous solutions by Fe_3O_4-stabilized Fe0 nanoparticles, J. Hazard. Mater. 172 (2009) 1640–1645.

[123] X.-F. Lu, L.-F. Gu, J.-W. Wang, J.-X. Wu, P.-Q. Liao, G.-R. Li, Bimetal-Organic Framework Derived $CoFe_2O_4$/C Porous Hybrid Nanorod Arrays as High-Performance Electrocatalysts for Oxygen Evolution Reaction, Adv. Mater. 29 (2017) 1604437.

[124] J. Zhou, Y. Wang, J. Wang, W. Qiao, D. Long, L. Ling, Effective removal of hexavalent chromium from aqueous solutions by adsorption on mesoporous carbon microspheres, J. Colloid Interface Sci. 462 (2016) 200–207.

[125] Y. Zou, X. Wang, A. Khan, P. Wang, Y. Liu, A. Alsaedi, T. Hayat, X. Wang, Environmental remediation and application of nanoscale zero-valent iron and its composites for the removal of heavy metal ions: a review, Environ. Sci. Technol. 50 (2016) 7290–7304.

[126] Z. Wang, J. Yang, Y. Li, Q. Zhuang, J. Gu, In situ Carbothermal Synthesis of Nanoscale Zero-Valent Iron Functionalized Porous Carbon from Metal-Organic Frameworks for Efficient Detoxification of Chromium (VI), Eur. J. Inorg. Chem. 2018 (2018) 23–30.

[127] H. Dong, J. Deng, Y. Xie, C. Zhang, Z. Jiang, Y. Cheng, K. Hou, G. Zeng, Stabilization of nanoscale zero-valent iron (nZVI) with modified biochar for Cr(VI) removal from aqueous solution, J. Hazard. Mater. 332 (2017) 79–86.

[128] X.-D. Du, C.-C. Wang, J.-G. Liu, X.-D. Zhao, J. Zhong, Y.-X. Li, J. Li, P. Wang, Extensive and selective adsorption of ZIF-67 towards organic dyes: performance and mechanism, J. Colloid Interface Sci. 506 (2017) 437–441.

[129] R.M. Cespón-Romero, M.C. Yebra-Biurrun, M.P. Bermejo-Barrera, Preconcentration and speciation of chromium by the determination of total chromium and chromium(III) in natural waters by flame atomic absorption spectrometry with a chelating ion-exchange flow injection system, Anal. Chim. Acta 327 (1996) 37–45.

[130] C. Zhao, Z. Wang, X. Li, X. Yi, H. Chu, X. Chen, C.-C. Wang, Facile fabrication of BUC-21/$Bi_{24}O_{31}Br_{10}$ composites for enhanced photocatalytic Cr(VI) reduction under white light, Chem. Eng. J. 389 (2020) 123431.

[131] M. Wang, Y. Zeng, G. Dong, C. Wang, Br-doping of g-C_3N_4 towards enhanced photocatalytic performance in Cr(VI) reduction, Chin. J. Catal. 41 (2020) 1498–1510.

[132] G. Liu, G. Dong, Y. Zeng, C. Wang, The photocatalytic performance and active sites of g-C_3N_4 effected by the coordination doping of Fe(III), Chin. J. Catal. 41 (2020) 1564–1572.

[133] P. Cieśla, P. Kocot, P. Mytych, Z. Stasicka, Homogeneous photocatalysis by transition metal complexes in the environment, J. Mol. Catal. A: Chem. 224 (2004) 17–33.

[134] X. Du, X. Yi, P. Wang, J. Deng, C.-C. Wang, Enhanced photocatalytic Cr(VI) reduction and diclofenac sodium degradation under simulated sunlight irradiation over MIL-100(Fe)/g-C_3N_4 heterojunctions, Chin. J. Catal. 40 (2019) 70–79.

[135] L. Wang, N. Wang, L. Zhu, H. Yu, H. Tang, Photocatalytic reduction of Cr (VI) over different TiO_2 photocatalysts and the effects of dissolved organic species, J. Hazard. Mater. 152 (2008) 93–99.

[136] K. Parida, K.G. Mishra, S.K. Dash, Adsorption of toxic metal ion Cr (VI) from aqueous state by TiO_2-MCM-41: Equilibrium and kinetic studies, J. Hazard. Mater. 241 (2012) 395–403.

[137] A. Hernández-Gordillo, F. Tzompantzi, R. Gómez, Enhanced photoreduction of Cr (VI) using ZnS (en) 0.5 hybrid semiconductor, Catal. Commun. 19 (2012) 51–55.

[138] A. Hernández-Gordillo, C. García-Mendoza, M. Alvarez-Lemus, R. Gómez, Photocatalytic reduction of Cr (VI) by using stacked ZnS layers of ZnS (en) x complex, J. Environ. Chem. Eng. 3 (2015) 3048–3054.

[139] M. Shirzad Siboni, M. Samadi, J. Yang, S. Lee, Photocatalytic reduction of Cr (VI) and Ni (II) in aqueous solution by synthesized nanoparticle ZnO under ultraviolet light irradiation: a kinetic study, Environ. Technol. 32 (2011) 1573–1579.

[140] M. Qamar, M. Gondal, Z. Yamani, Laser-induced efficient reduction of Cr (VI) catalyzed by ZnO nanoparticles, J. Hazard. Mater. 187 (2011) 258–263.

[141] X. An, C.Y. Jimmy, F. Wang, C. Li, Y. Li, One-pot synthesis of In_2S_3 nanosheets/graphene composites with enhanced visible-light photocatalytic activity, Appl. Catal. B 129 (2013) 80–88.

[142] S. Nandy, S. Ch, Synthesis of CdS/CeO_2 hetero nanostructures for Photocatalytic H_2 production and simultaneous Removal of phenol and Cr (VI), Indian Institute of Technology, Hyderabad, 2014.

[143] C. Yu, D. Mao, F. Xia, X. Huang, J. Li, W. Liu, D. Fang, Formation of SnS_2/Ni_2S_3 heterojunction on three-dimensional nickelframework for treating chromium (VI)-containing wastewater, Mater. Res. Express 4 (2017) 115023.

[144] B. Ma, P.-Y. Guan, Q.-Y. Li, M. Zhang, S.-Q. Zang, MOF-Derived Flower-like MoS_2@TiO_2 Nanohybrids with Enhanced Activity for Hydrogen Evolution, ACS Appl. Mater. Interfaces 8 (2016) 26794–26800.

[145] G.-C. Li, M. Liu, M.-K. Wu, P.-F. Liu, Z. Zhou, S.-R. Zhu, R. Liu, L. Han, MOF-derived self-sacrificing route to hollow NiS_2/ZnS nanospheres for high performance supercapacitors, RSC Adv. 6 (2016) 103517–103522.

[146] S.J. Yang, J.H. Im, T. Kim, K. Lee, C.R. Park, MOF-derived ZnO and ZnO@C composites with high photocatalytic activity and adsorption capacity, J. Hazard. Mater. 186 (2011) 376–382.

[147] M. Lan, R.-M. Guo, Y. Dou, J. Zhou, A. Zhou, J.-R. Li, Fabrication of porous Pt-doping heterojunctions by using bimetallic MOF template for photocatalytic hydrogen generation, Nano Energy 33 (2017) 238–246.

[148] C.-H. Lai, M.-Y. Lu, L.-J. Chen, Metal sulfide nanostructures: synthesis, properties and applications in energy conversion and storage, J. Mater. Chem. 22 (2012) 19–30.

[149] A.P. Gaikwad, D. Tyagi, C.A. Betty, R. Sasikala, Photocatalytic and photo electrochemical properties of cadmium zinc sulfide solid solution in the presence of Pt and RuS_2 dual co-catalysts, Appl. Catal. A 517 (2016) 91–99.

[150] J. Zhang, J. Yu, Y. Zhang, Q. Li, J.R. Gong, Visible Light Photocatalytic H_2-Production Activity of CuS/ZnS Porous Nanosheets Based on Photoinduced Interfacial Charge Transfer, Nano Lett. 11 (2011) 4774–4779.

[151] J.-S. Hu, L.-L. Ren, Y.-G. Guo, H.-P. Liang, A.-M. Cao, L.-J. Wan, C.-L. Bai, Mass Production and High Photocatalytic Activity of ZnS Nanoporous Nanoparticles, Angew. Chem. Int. Ed. 44 (2005) 1269–1273.

[152] Y. Huang, W. Fan, B. Long, H. Li, F. Zhao, Z. Liu, Y. Tong, H. Ji, Visible light Bi_2S_3/Bi_2O_3/$Bi_2O_2CO_3$ photocatalyst for effective degradation of organic pollutions, Appl. Catal. B 185 (2016) 68–76.

[153] Z. Ren, L. Li, B. Liu, X. Liu, Z. Li, X. Lei, C. Li, Y. Gong, L. Niu, L. Pan, Cr(VI) reduction in presence of ZnS/RGO photocatalyst under full solar spectrum radiation from UV/vis to near-infrared light, Catal. Today 315 (2018) 46–51.

[154] S.K. Maji, A.K. Dutta, D.N. Srivastava, P. Paul, A. Mondal, B. Adhikary, Effective photocatalytic degradation of organic pollutant by ZnS nanocrystals synthesized via thermal decomposition of single-source precursor, Polyhedron 30 (2011) 2493–2498.

[155] F.A. La Porta, M.M. Ferrer, Y.V.B. de Santana, C.W. Raubach, V.M. Longo, J.R. Sambrano, E. Longo, J. Andrés, M.S. Li, J.A. Varela, Synthesis of wurtzite ZnS nanoparticles using the microwave assisted solvothermal method, J. Alloy. Compd. 556 (2013) 153–159.

[156] Y. Jiang, X.M. Meng, J. Liu, Z.Y. Xie, C.S. Lee, S.T. Lee, Hydrogen-Assisted Thermal Evaporation Synthesis of ZnS Nanoribbons on a Large Scale, Adv. Mater. 15 (2003) 323–327.

[157] R.D. Engelken, S. Ali, C. Lip Ngin, C. Brinkley, K. Turner, C. Hester, Study and development of a generic electrochemical ion-exchange process to form MxS optoelectronic materials from ZnS precursor films formed by chemical-precipitation solution deposition, Mater. Lett. 10 (1990) 264–274.

[158] H. Fu, Z. Wang, X. Wang, P. Wang, C.-C. Wang, Formation mechanism of rod-like ZIF-L and fast phase transformation from ZIF-L to ZIF-8 with morphology changes controlled by polyvinylpyrrolidone and ethanol, CrystEngComm 20 (2018)

1473–1477.
[159] H. Fu, X. Wang, P. Wang, Z. Wang, H. Ren, C.-C. Wang, Enhanced acetone sensing performance of Au nanoparticle modified porous tube-like ZnO derived from rod-like ZIF-L, Dalton Trans. 47 (2018) 9014–9020.
[160] Z. Jiang, H. Sun, Z. Qin, X. Jiao, D. Chen, Synthesis of novel ZnS nanocages utilizing ZIF-8 polyhedral template, Chem. Commun. 48 (2012) 3620–3622.
[161] J. Qiu, X.-F. Zhang, X. Zhang, Y. Feng, Y. Li, L. Yang, H. Lu, J. Yao, Constructing $Cd_{0.5}Zn_{0.5}S$@ZIF-8 nanocomposites through self-assembly strategy to enhance Cr (VI) photocatalytic reduction, J. Hazard. Mater. 349 (2018) 234–241.
[162] G. Blázquez, F. Hernáinz, M. Calero, M. Martín-Lara, G. Tenorio, The effect of pH on the biosorption of Cr (III) and Cr (VI) with olive stone, Chem. Eng. J. 148 (2009) 473–479.
[163] X.-H. Yi, F.-X. Wang, X.-D. Du, H. Fu, C.-C. Wang, Highly efficient photocatalytic Cr (VI) reduction and organic pollutants degradation of two new bifunctional 2D Cd/Co-based MOFs, Polyhedron 152 (2018) 216–224.
[164] S. Deng, R. Bai, Removal of trivalent and hexavalent chromium with aminated polyacrylonitrile fibers: performance and mechanisms, Water Res. 38 (2004) 2424–2432.
[165] O. Ajouyed, C. Hurel, M. Ammari, L.B. Allal, N. Marmier, Sorption of Cr (VI) onto natural iron and aluminum (oxy) hydroxides: effects of pH, ionic strength and initial concentration, J. Hazard. Mater. 174 (2010) 616–622.
[166] C. Zhao, Z. Wang, X. Li, X. Yi, H. Chu, X. Chen, C.-C. Wang, Facile fabrication of BUC-21/$Bi_{24}O_{31}Br_{10}$ composites for enhanced photocatalytic Cr (VI) reduction under white light, Chem. Eng. J. 123431 (2019).
[167] Y. Liu, L. Deng, Y. Chen, F. Wu, N. Deng, Simultaneous photocatalytic reduction of Cr(VI) and oxidation of bisphenol A induced by Fe(III)–OH complexes in water, J. Hazard. Mater. 139 (2007) 399–402.
[168] W. Zhao, J. Zhang, F. Zhu, F. Mu, L. Zhang, B. Dai, J. Xu, A. Zhu, C. Sun, D.Y.C. Leung, Study the photocatalytic mechanism of the novel Ag/p-Ag_2O/n-$BiVO_4$ plasmonic photocatalyst for the simultaneous removal of BPA and chromium(VI), Chem. Eng. J. 361 (2019) 1352–1362.
[169] R. Yuan, C. Yue, J. Qiu, F. Liu, A. Li, Highly efficient sunlight-driven reduction of Cr (VI) by TiO_2@ NH_2-MIL-88B (Fe) heterostructures under neutral conditions, Appl. Catal. B 251 (2019) 229–239.
[170] X. Fu, X. Wang, Z. Chen, Z. Zhang, Z. Li, D.Y.C. Leung, L. Wu, X. Fu, Photocatalytic performance of tetragonal and cubic β-In_2S_3 for the water splitting under visible light irradiation, Appl. Catal. B 95 (2010) 393–399.
[171] X. An, J.C. Yu, F. Wang, C. Li, Y. Li, One-pot synthesis of In_2S_3 nanosheets/graphene composites with enhanced visible-light photocatalytic activity, Appl. Catal. B 129 (2013) 80–88.
[172] A. Timoumi, H. Bouzouita, M. Kanzari, B. Rezig, Fabrication and characterization of In_2S_3 thin films deposited by thermal evaporation technique, Thin Solid Films 480–481 (2005) 124–128.
[173] Y. Wang, D. Cao, M. Liu, X. Zhao, Insights into heterogeneous catalytic activation of peroxymonosulfate by Pd/g-C_3N_4: the role of superoxide radical and singlet oxygen, Catal. Commun. 102 (2017) 85–88.
[174] D.-D. Chen, X.-H. Yi, C. Zhao, H. Fu, P. Wang, C.-C. Wang, Polyaniline modified MIL-100(Fe) for enhanced photocatalytic Cr(VI) reduction and tetracycline degradation under white light, Chemosphere 245 (2020) 125659.
[175] X. Yu, T.J. Marks, A. Facchetti, Metal oxides for optoelectronic applications, Nat. Mater. 15 (2016) 383–396.
[176] M.M. Khan, S.F. Adil, A. Al-Mayouf, Metal oxides as photocatalysts, Elsevier, 2015.
[177] J.-H. Sun, S.-Y. Dong, Y.-K. Wang, S.-P. Sun, Preparation and photocatalytic property of a novel dumbbell-shaped ZnO microcrystal photocatalyst, J. Hazard. Mater. 172 (2009) 1520–1526.
[178] X. Bai, L. Wang, Y. Zhu, Visible Photocatalytic Activity Enhancement of $ZnWO_4$ by Graphene Hybridization, ACS Catal. 2 (2012) 2769–2778.
[179] J. Wang, P. Liu, X. Fu, Z. Li, W. Han, X. Wang, Relationship between Oxygen Defects and the Photocatalytic Property of ZnO Nanocrystals in Nafion Membranes, Langmuir 25 (2009) 1218–1223.
[180] R.A.W. Johnstone, A.H. Wilby, I.D. Entwistle, Heterogeneous catalytic transfer hydrogenation and its relation to other methods for reduction of organic compounds, Chem. Rev. 85 (1985) 129–170.
[181] A. Dandapat, D. Jana, G. De, Pd nanoparticles supported mesoporous γ-Al_2O_3 film as a reusable catalyst for reduction of toxic CrVI to CrIII in aqueous solution, Appl. Catal. A 396 (2011) 34–39.
[182] H. Chen, Y. Shao, Z. Xu, H. Wan, Y. Wan, S. Zheng, D. Zhu, Effective catalytic reduction of Cr(VI) over TiO_2 nanotube supported Pd catalysts, Appl. Catal. B 105 (2011) 255–262.
[183] G. Brieger, T.J. Nestrick, Catalytic transfer hydrogenation, Chem. Rev. 74 (1974) 567–580.
[184] X. Zhou, Z. Chen, D. Yan, H. Lu, Deposition of Fe–Ni nanoparticles on polyethyleneimine-decorated graphene oxide and application in catalytic dehydrogenation of ammonia borane, J. Mater. Chem. 22 (2012) 13506–13516.
[185] E. Heracleous, A.F. Lee, K. Wilson, A.A. Lemonidou, Investigation of Ni-based alumina-supported catalysts for the oxidative dehydrogenation of ethane to ethylene: structural characterization and reactivity studies, J. Catal. 231 (2005) 159–171.
[186] Y.-C. Zhou, P. Wang, H. Fu, C. Zhao, C.-C. Wang, Ternary Ag/Ag_3PO_4/MIL-125-NH_2 Z-scheme heterojunction for boosted photocatalytic Cr(VI) cleanup under visible light, Chin. Chem. Lett. (2020).
[187] A. Dhakshinamoorthy, H. Garcia, Catalysis by metal nanoparticles embedded on metal–organic frameworks, Chem. Soc. Rev. 41 (2012) 5262–5284.
[188] I. Jiménez-Morales, S. Cavaliere, D. Jones, J. Rozière, Strong metal–support interaction improves activity and stability of Pt electrocatalysts on doped metal oxides, Phys. Chem. Chem. Phys. 20 (2018) 8765–8772.
[189] C. Goyhenex, G. Tréglia, Unified picture of d-band and core-level shifts in transition metal alloys, Physical Review B 83 (2011) 075101.
[190] Y. Liu, H. Jiang, Y. Zhu, X. Yang, C. Li, Transition metals (Fe Co, and Ni) encapsulated in nitrogen-doped carbon nanotubes as bi-functional catalysts for oxygen electrode reactions, J. Mater. Chem. A 4 (2016) 1694–1701.
[191] J. Kang, H. Zhang, X. Duan, H. Sun, X. Tan, S. Liu, S. Wang, Magnetic Ni-Co alloy encapsulated N-doped carbon nanotubes for catalytic membrane degradation of emerging contaminants, Chem. Eng. J. 362 (2019) 251–261.
[192] Y. Yao, C. Lian, G. Wu, Y. Hu, F. Wei, M. Yu, S. Wang, Synthesis of "sea urchin"-like carbon nanotubes/porous carbon superstructures derived from waste biomass for treatment of various contaminants, Appl. Catal. B 219 (2017) 563–571.
[193] L. Tang, G.-D. Yang, G.-M. Zeng, Y. Cai, S.-S. Li, Y.-Y. Zhou, Y. Pang, Y.-Y. Liu, Y. Zhang, B. Luna, Synergistic effect of iron doped ordered mesoporous carbon on adsorption-coupled reduction of hexavalent chromium and the relative mechanism study, Chem. Eng. J. 239 (2014) 114–122.
[194] F. Zou, X. Hu, Z. Li, L. Qie, C. Hu, R. Zeng, Y. Jiang, Y. Huang, MOF-Derived Porous ZnO/$ZnFe_2O_4$/C Octahedra with Hollow Interiors for High-Rate Lithium-Ion Batteries, Adv. Mater. 26 (2014) 6622–6628.
[195] X. Wang, Z. Ma, L. Chai, L. Xu, Z. Zhu, Y. Hu, J. Qian, S. Huang, MOF derived N-doped carbon coated CoP particle/carbon nanotube composite for efficient oxygen evolution reaction, Carbon 141 (2019) 643–651.
[196] X. Bai, J. Liu, Q. Liu, R. Chen, X. Jing, B. Li, J. Wang, In-Situ Fabrication of MOF-Derived Co − Co Layered Double Hydroxide Hollow Nanocages/Graphene Composite: A Novel Electrode Material with Superior Electrochemical Performance, Chem. Eur. J. 23 (2017) 14839–14847.
[197] J. Yuan, Q. Liu, S. Li, Y. Lu, S. Jin, K. Li, H. Chen, H. Zhang, Metal organic framework (MOF)-derived carbonaceous Co_3O_4/Co microframes anchored on RGO with enhanced electromagnetic wave absorption performances, Synth. Met. 228 (2017) 32–40.
[198] D. Ji, H. Zhou, Y. Tong, J. Wang, M. Zhu, T. Chen, A. Yuan, Facile fabrication of MOF-derived octahedral CuO wrapped 3D graphene network as binder-free anode for high performance lithium-ion batteries, Chem. Eng. J. 313 (2017) 1623–1632.
[199] J. Xu, W. Zhang, Y. Chen, H. Fan, D. Su, G. Wang, MOF-derived porous N-Co_3O_4@N–C nanododecahedra wrapped with reduced graphene oxide as a high capacity cathode for lithium–sulfur batteries, J. Mater. Chem. A 6 (2018) 2797–2807.
[200] J. Feng, H. Zhou, J. Wang, T. Bian, J. Shao, A. Yuan, MoS_2 supported on MOF-derived carbon with core-shell structure as efficient electrocatalysts for hydrogen evolution reaction, Int. J. Hydrogen Energy 43 (2018) 20538–20545.
[201] S. Mandegarzad, J.B. Raoof, S.R. Hosseini, R. Ojani, MOF-derived Cu-Pd/nanoporous carbon composite as an efficient catalyst for hydrogen evolution reaction: A comparison between hydrothermal and electrochemical synthesis, Appl. Surf. Sci. 436 (2018) 451–459.
[202] R. Li, S. Wu, X. Wan, H. Xu, Y. Xiong, Cu/TiO_2 octahedral-shell photocatalysts derived from metal–organic framework@ semiconductor hybrid structures, Inorg. Chem. Front. 3 (2016) 104–110.
[203] X. Ma, X. Zhou, Y. Gong, N. Han, H. Liu, Y. Chen, MOF-derived hierarchical ZnO/$ZnFe_2O_4$ hollow cubes for enhanced acetone gas-sensing performance, RSC Adv. 7 (2017) 34609–34617.
[204] C. Palomino Cabello, M.F.F. Picó, F. Maya, M. del Rio, G. Turnes Palomino, UiO-66 derived etched carbon/polymer membranes: High-performance supports for the extraction of organic pollutants from water, Chem. Eng. J. 346 (2018) 85–93.
[205] C.-C. Wang, Y.-S. Ho, Research trend of metal–organic frameworks: a bibliometric analysis, Scientometrics 109 (2016) 481–513.
[206] H. Wang, X. Yuan, Y. Wu, G. Zeng, X. Chen, L. Leng, Z. Wu, L. Jiang, H. Li, Facile synthesis of amino-functionalized titanium metal-organic frameworks and their superior visible-light photocatalytic activity for Cr (VI) reduction, J. Hazard. Mater. 286 (2015) 187–194.
[207] X.H. Yi, F.X. Wang, X.D. Du, P. Wang, C.C. Wang, Facile fabrication of BUC-21/g-C_3N_4 composites and their enhanced photocatalytic Cr (VI) reduction performances under simulated sunlight, Appl. Organomet. Chem. 33 (2019) e4621.
[208] X.-H. Yi, S.-Q. Ma, X.-D. Du, C. Zhao, H. Fu, P. Wang, C.-C. Wang, The facile fabrication of 2D/3D Z-scheme g-C_3N_4/UiO-66 heterojunction with enhanced photocatalytic Cr (VI) reduction performance under white light, Chem. Eng. J. 375 (2019) 121944.
[209] W. Zhao, J. Zhang, F. Zhu, F. Mu, L. Zhang, B. Dai, J. Xu, A. Zhu, C. Sun, D.Y. Leung, Study the photocatalytic mechanism of the novel Ag/p-Ag_2O/n-$BiVO_4$ plasmonic photocatalyst for the simultaneous removal of BPA and chromium (VI), Chem. Eng. J. 361 (2019) 1352–1362.
[210] C. Yu, Z. Wu, R. Liu, D.D. Dionysiou, K. Yang, C. Wang, H. Liu, Novel fluorinated Bi_2MoO_6 nanocrystals for efficient photocatalytic removal of water organic pollutants under different light source illumination, Appl. Catal. B 209 (2017) 1–11.